# 5 Porosity Logs

Rock porosity can be obtained from the sonic log, the density log, or the neutron log. For all these devices, the tool response is affected by the formation porosity, fluid, and matrix. If the fluid and matrix effects are known or can be determined, the tool response can be related to porosity. Therefore, these devices are often referred to as porosity logs.

All three logging techniques respond to the characteristics of the rock immediately adjacent to the borehole. Their depth of investigation is very shallow — only a few inches or less — and therefore generally within the flushed zone.

Other petrophysical measurements, such as microresistivity or nuclear magnetism or electromagnetic propagation, are sometimes used to determine porosity. However, these devices are also greatly influenced by the fluid saturating the rock pores. For that reason, they are discussed elsewhere.

## SONIC LOGS

In its simplest form, a sonic tool consists of a transmitter that emits a sound pulse and a receiver that picks up and records the pulse as it passes the receiver. The sonic log is simply a recording versus depth of the time, $t$, required for a sound wave to traverse 1 ft of formation. Known as the interval transit time, transit time, $\Delta t$ or slowness, $t$ is the reciprocal of the velocity of the sound wave. The interval transit time for a given formation depends upon its lithology and porosity. This dependence upon porosity, when the lithology is known, makes the sonic log very useful as a porosity log. Integrated sonic transit times are also helpful in interpreting seismic records. The sonic log can be run simultaneously with many other services.

### Principle

The propagation of sound in a borehole is a complex phenomenon. It is governed by the mechanical properties of several separate acoustical domains. These include the formation, the borehole fluid column, and the logging tool itself.

The sound emanated from the transmitter impinges on the borehole wall. This establishes compressional and shear waves within the formation, surface waves along the borehole wall, and guided waves within the fluid column.

In the case of well logging, the borehole wall, formation bedding, borehole rugosity, and fractures can all represent significant acoustic discontinuities. Therefore, the phenomena of wave refraction, reflection, and conversion lead to the presence of many acoustic waves in the borehole when a sonic log is being run. It is not surprising, in view of these considerations, that many acoustic energy arrivals are seen by the receivers of a sonic logging tool. The more usual energy arrivals are shown in the acoustic waveform displays of Fig. 5-1. These waveforms were recorded with an array of eight receivers located 8 to 11½ ft from the transmitter. The various wave packets have been labeled. Although the wave packets are not totally separated in time at this spacing, the distinct changes corresponding to the onset of the formation compressional and shear arrivals and the Stoneley arrival can be observed.

The first arrival or compressional wave is one that has traveled from the transmitter to the formation as a fluid pressure wave, has been refracted at the borehole wall, has traveled within the formation at the compressional wave velocity of the formation, and has traveled back to the receiver as a fluid pressure wave.

The shear wave is one that has traveled from the transmitter to the formation as a fluid pressure wave, has traveled within the formation at the shear wave velocity of the formation, and has traveled back to the receiver as a fluid pressure wave.

The mud wave (not strongly evident in these wavetrains) is one that has traveled directly from transmitter to receiver in the mud column at the compressional wave velocity of the borehole fluid.

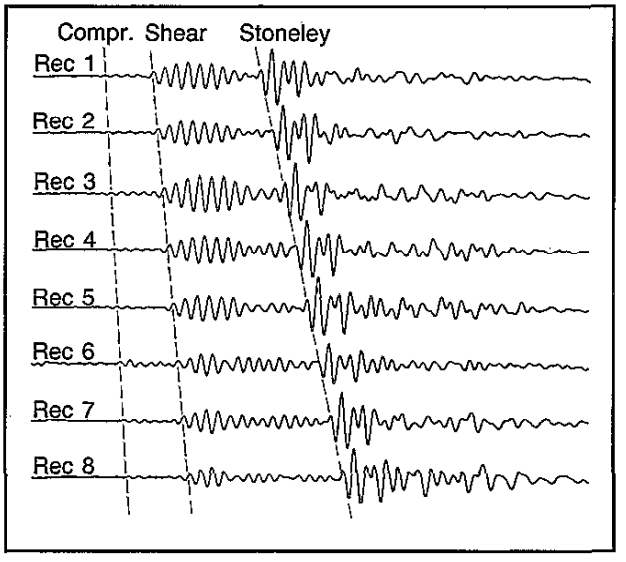


Fig. 5-1—Example waveforms from the eight-receiver Array-Sonic tool.

The Stoneley wave is one of large amplitude that has traveled from transmitter to receiver with a velocity less than that of the compressional waves in the borehole fluid. The velocity of the Stoneley wave is dependent upon the frequency of the sound pulse, hole diameter, formation shear velocity, densities of the formation and fluid, and fluid compressional wave velocity.

**Equipment**

There are currently three sonic tools in use: the BHC* borehole compensated sonic tool, the LSS* long-spaced sonic tool, and the Array-Sonic* tool. Although the entire sonic waveform can now be recorded with any of these tools, only the Array-Sonic tool has been designed to provide full-waveform recording as a standard feature.

Nearly all BHC logs recorded in the past provide only a measurement of formation compressional interval transit time, $t$, accomplished through first motion detection at the receiver. In other words, the receiver triggers on the first arrival of compressional energy.

As shown in Fig. 5-2, the BHC system uses one transmitter above and one transmitter below two pairs of sonic receivers. This sonde substantially reduces the spurious effects of hole-size changes and errors from sonde tilt. When one of the transmitters is pulsed the time elapsed between detection of the first arrival at the two corresponding receivers is measured.

The speed of sound in the sonic sonde and in the drilling mud is less than that in the formations. Accordingly, the first arrivals of sound energy at the receivers correspond to sound-travel paths in the formation near the borehole wall.

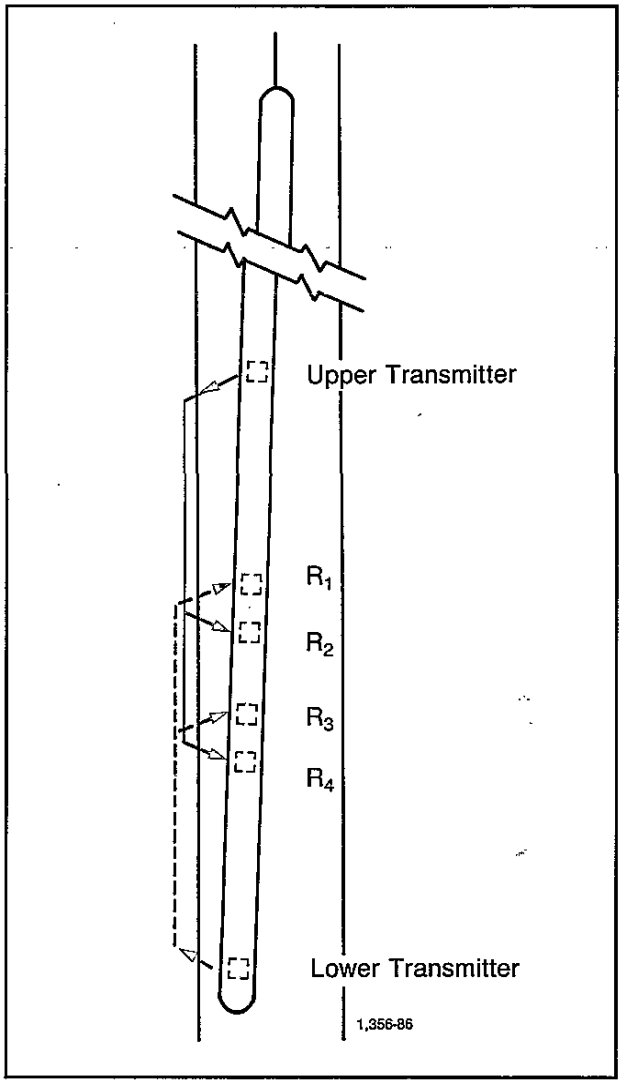


Fig. 5-2—Schematic of BHC sonde, showing ray paths for the two transmitter-receiver sets. Averaging the two Δt measurements cancels errors from sonde tilt and hole-size changes. (Ref. 2)

The BHC tool transmitters are pulsed alternately, and $t$ values are read on alternate pairs of receivers. The $t$ values from the two sets of receivers are averaged automatically by a computer at the surface for borehole compensation. The computer also integrates the transit-time readings to obtain total travel times (see Fig. 5-3).

Sometimes the first arrival, although strong enough to trigger the receiver nearer the transmitter, may be too weak by the time it reaches the far receiver to trigger it. Instead, the far receiver may be triggered by a different, later arrival in the sonic wave train, and the travel time measured on this pulse cycle will then be too large. When this occurs, the sonic curve shows a very abrupt and large

*Mark of Schlumberger

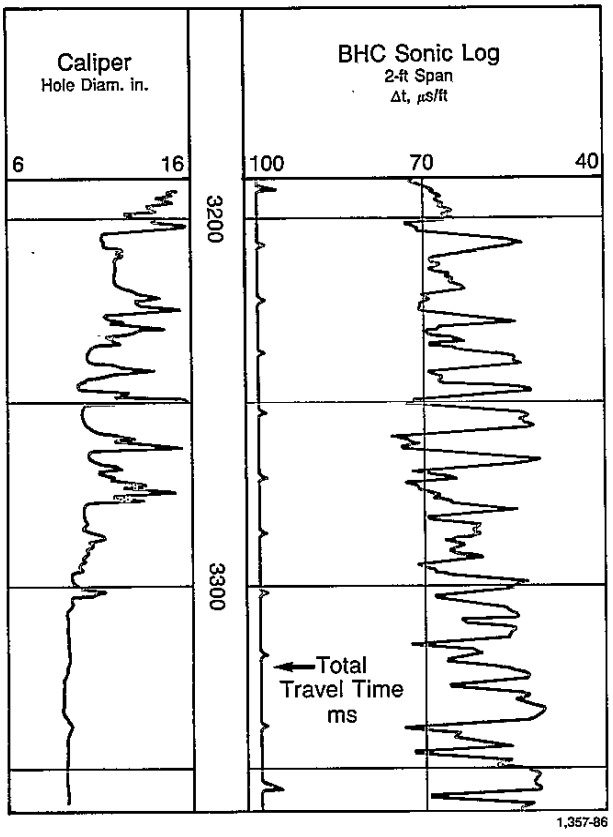


Fig. 5-3—Presentation of sonic log. (Ref. 3)

excursion towards a higher $t$ value; this is known as cycle skipping. Such skipping is more likely to occur when the signal is strongly attenuated by unconsolidated formations, formation fractures, gas saturation, aerated muds, or rugose or enlarged borehole sections.

In early studies of velocity logging, the rock surrounding the wellbore was regarded as an infinite homogeneous medium for the propagation of sound waves. It is now apparent that in some shales a lateral velocity gradient exists. Sound waves travel at lower speeds near the borehole; at some greater distance from the borehole, they propagate at the true speed of sound in the shale. Similar variations may exist in the radial velocity profile in some unconsolidated rocks and in permafrost.

In large-diameter boreholes, it is possible to have a mud wave arrival at the near receiver before the formation signal. This problem is particularly prevalent at shallower depths where sonic logs are often run for seismic purposes.

In all these cases, a sonic tool with long spacing is required to provide a correct measurement of the velocity in the nonaltered zone. When the receivers are far enough from the transmitter, the first arrival is not the refracted ray traveling just inside the borehole wall but a wave penetrating beyond the borehole into the faster nonaltered zone.

LSS sonic tools, with transmitter-receiver spacings of 8 ft and 10 ft or 10 ft and 12 ft, are available. They measure the interval transit time of the formation at a much greater depth into the formation than the usual BHC sonic tool. This tool is more likely to yield a measurement free from the effects of formation alteration, relaxation damage (from drilling process), and enlarged borehole. These more accurate measurements are always desirable when the sonic data are to be used for seismic purposes. Fig. 5-4 compares the transit time recorded with an LSS tool to that from a standard-spacing tool in a formation with alteration.

Using the standard BHC system for borehole compensation with an LSS sonde would make the tool excessively long. An alternate solution called "depth-derived" borehole compensation is used.

The LSS sonde has two transmitters and two receivers arranged as shown in Fig. 5-5. Readings are taken at two different depth positions of the sonde: once when the two receivers straddle the measure point depth and once when the two transmitters straddle the measure point depth.

$$\text{First } t \text{ reading} = T_1 \rightarrow R_1 - T_1 \rightarrow R_2$$

$$\text{Second } t \text{ reading} = T_1 \rightarrow R_2 - T_2 \rightarrow R_2$$

The first $t$ reading is memorized until the sonde has reached the position to make the second $t$ reading, then both are averaged to obtain the borehole compensated measurement.

$$t = \frac{\text{memorized first } t \text{ reading} + \text{second } t \text{ reading}}{2 \times \text{span}}$$

where span is the distance (2 ft) between a pair of receivers.

Assuming the two sonde position depths are accurately known and the sonde tilting is similar for the two positions, the depth-derived borehole compensated system is equivalent to the standard BHC system. Use of the upper transmitter and receiver yields an 8-ft—10-ft sonic $t$ measurement, and use of the lower transmitter and receiver yields a 10-ft—12-ft sonic $t$ measurement.

The Array-Sonic service provides all measurements of the BHC and LSS logs and, in addition, provides several other features. The tool contains two broadband (5 to 18 kHz) piezoelectric transmitters spaced 2 ft apart. Two piezoelectric receivers are located 3 ft and 5 ft from the upper transmitter. These receivers have a dual role. In open hole, they are used in conjunction with the two transmitters to make standard short-spaced 3-ft—5-ft and 5-ft—7-ft depth-derived, borehole-compensated $t$ logs. In cased wells, they are used to make standard 3-ft ce-

ment bond logs (CBL) and 5-ft Variable Density* logs (VDL).

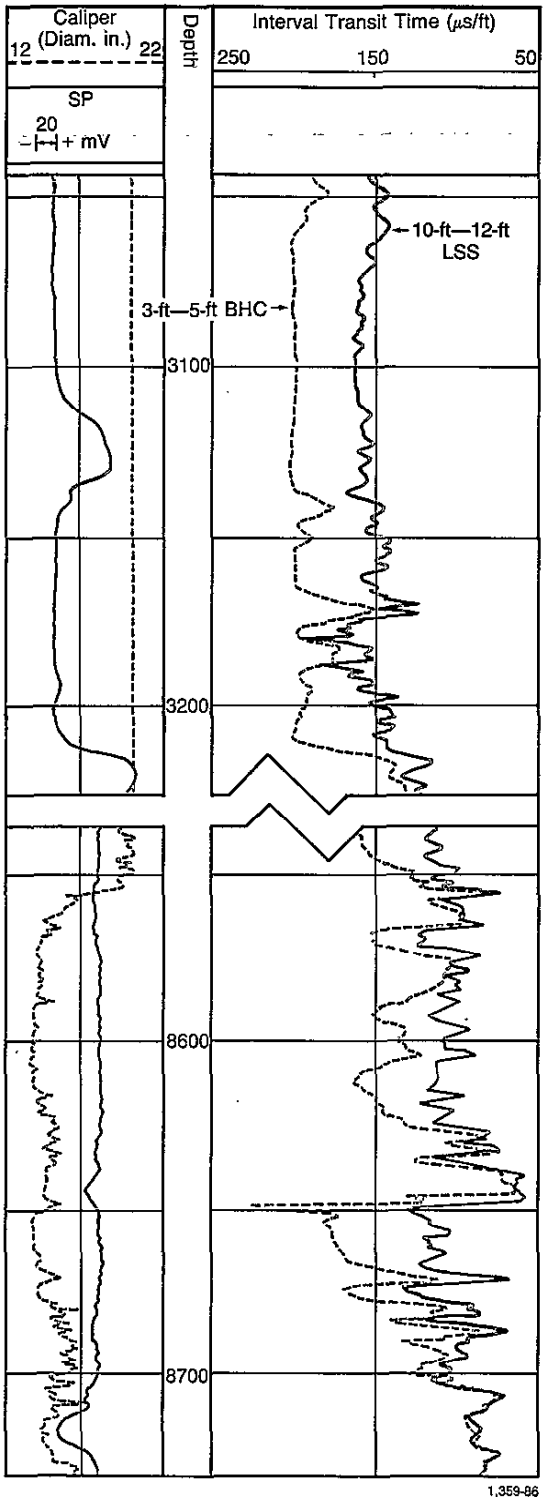


Fig. 5-4—Comparison of LSS and BHC sonic logs in enlarged holes.

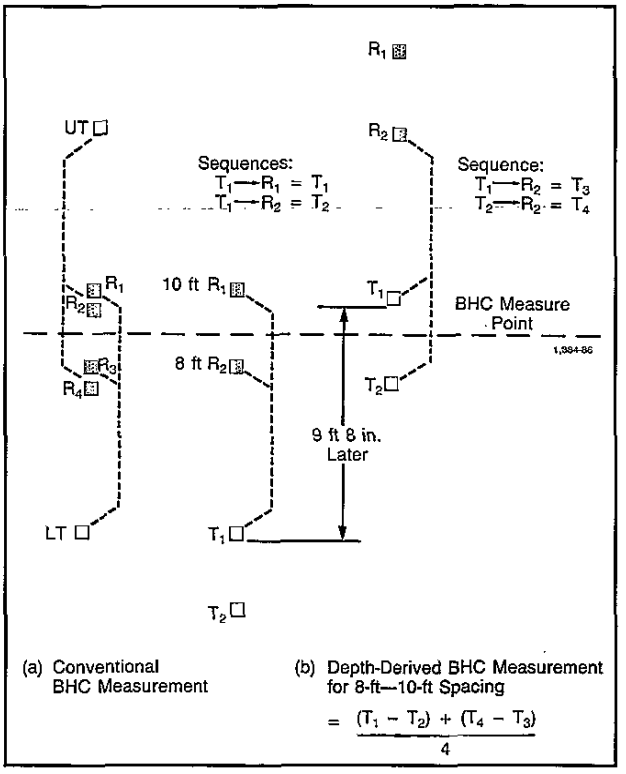


Fig. 5-5—Depth-derived compensation for long-spaced sonic tool.

The Array-Sonic tool (Fig. 5-6) also contains an array of eight wideband piezoelectric receivers. The receivers are spaced 6 in. apart with the closest receiver 8 ft from the upper transmitter. Two of these receivers, Receivers 1 and 5, spaced 2 ft apart, can be used for making standard long-spaced 8-ft—10-ft and 10-ft—12-ft depth-derived borehole-compensated $t$ logs. Measurement hardware also exists, consisting of a closely spaced transmitter-receiver pair, to make a continuous mud $t$ log. Borehole fluid is drawn through this measurement section as the tool is moved during logging.

The eight-array receiver outputs and the two from the sonic sonde are multiplexed with the mud $t$ receiver output and transmitted to the surface in either analog or digital form. An example of a set of waveforms digitized from the eight-receiver array is shown in Fig. 5-1.

The array waveforms are processed at the wellsite with the CSU* surface instrumentation and array processor or at the computing center using a true full-waveform technique.

Rather than recording just the compressional wave component, a waveform-processing technique is used to find and analyze all propagating waves in the composite waveform. This slowness-time coherence technique (STC)

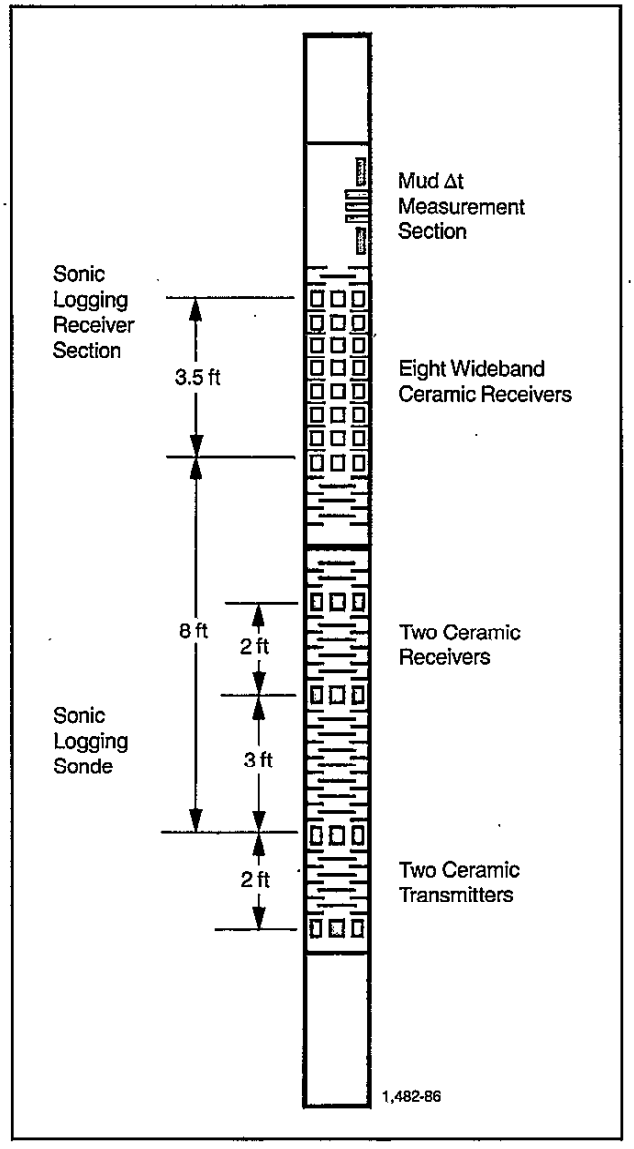


Fig. 5-6—Multipurpose sonic sonde configuration.

uses a semblance algorithm, similar to that employed in seismic processing, to detect arrivals that are coherent across the array of receiver waveforms and to estimate their interval transit time.

Applying this semblance algorithm to the waveforms of Fig. 5-1 produces the coherence map shown in Fig. 5-7. Regions of large coherence correspond to the compressional, shear, and Stoneley arrivals. The apex of each region defines the slowness of that wave. This process is repeated for each set of array waveforms acquired by the tool while moving up the hole and is used to produce a log. A typical log determined in this fashion is shown in Fig. 5-8. Compressional transit time, $t_c$; shear transit time, $t_s$; and Stoneley transit time, $t_{St}$, are presented. In a slow formation, the tool obtains real-time measurements of compressional, Stoneley, and mud wave velocities. Shear wave values are then derived from these velocities.

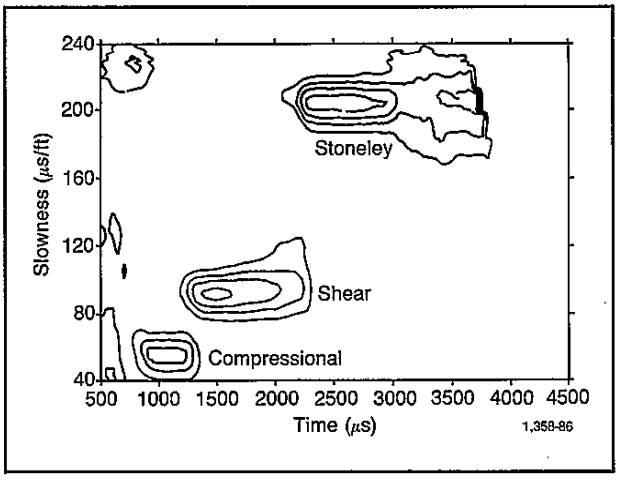


Fig. 5-7—Contour plot of the STC coherence function.

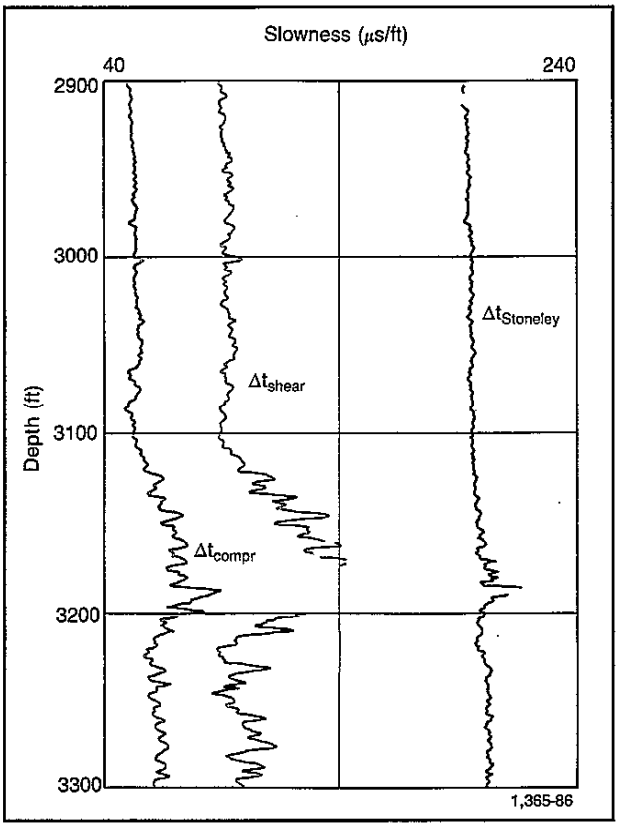


Fig. 5-8—Log of classified component slownesses.

Because of the number of receivers, the full-wavetrain recording, and the digital transmission, the Array-Sonic tool can provide a large amount of acoustic information. Among these data are:

- 3-ft—5-ft $t_c$ (first-motion compressional transit time)
- 5-ft—7-ft $t_c$
- 8-ft—10-ft $t_c$
- 10-ft—12-ft $t_c$
- $t_c$ (wavetrain-derived compressional transit time)
- $t_s$ (wavetrain-derived shear transit time)
- $t_{St}$ (wavetrain-derived Stoneley transit time)
- 6-in. $t_c$ (first-motion compressional transit time)
- Mud transit time
- Amplitude logging
- Energy analysis
- Frequency analysis
- $t_c$, $t_s$, and $t_{St}$ through casing
- CBL/VDL data through casing

### Log Presentation

Sonic velocities in common formation lithologies range from about 6,000 to 23,000 ft/sec. To avoid small decimal fractions the reciprocal of velocity, $t$, is recorded (English scale) in microseconds per foot ($\mu$s/ft) over a range from about 44 $\mu$s/ft for zero-porosity dense dolomite to about 190 $\mu$s/ft for water.

The interval transit time is usually recorded on a linear scale in Tracks 2 and 3 of the log (Fig. 5-3). The integrated travel time is given by a series of pips, usually recorded at the left edge of Track 2. Each small pip indicates an increase of 1 ms of the total travel time; a large pip is recorded every 10 ms. The travel time between two depths is obtained by simply counting the pips. The integrated travel time is useful for seismic purposes.

### Sonic Velocities In Formations

In sedimentary formations the speed of sound depends on many parameters; principally, it depends on the rock matrix material (sandstone, limestone, dolomite ...) and on the distributed porosity. Ranges of values of sonic velocity and transit time for common rock matrix materials and casing are listed in Table 5-1.

The values listed are for nonporous substances. Porosity decreases the velocity of sound through the rock material and, correspondingly, increases the interval transit time.

**Table 1**

| | $v_{ma}$(ft/sec) | $\Delta t_{ma}$($\mu$s/ft) | $\Delta t_{ma}$($\mu$s/ft) (commonly used) |
|---|---|---|---|
| **Sandstones** | 18,000-19,500 | 55.5-51.0 | 55.5 or 51.0 |
| **Limestones** | 21,000-23,000 | 47.6-43.5 | 47.5 |
| **Dolomites** | 23,000 | 43.5 | 43.5 |
| **Anhydrite** | 20,000 | 50.0 | 50.0 |
| **Salt** | 15,000 | 66.7 | 67.0 |
| **Casing (iron)** | 17,500 | 57.0 | 57.0 |

1,367-86

### Porosity Determination (Wyllie Time-Average Equation)

Consolidated and Compacted Sandstones

After numerous laboratory determinations, M.R.J. Wyllie proposed, for clean and consolidated formations with uniformly distributed small pores, a linear time-average or weighted-average relationship between porosity and transit time:

$$t_{LOG} = \phi\, t_f + (1 - \phi)\, t_{ma} \quad \text{(Eq. 5-1a)}$$

or

$$\phi = \frac{t_{LOG} - t_{ma}}{t_f - t_{ma}}, \quad \text{(Eq. 5-1b)}$$

where

$t_{LOG}$ is the reading on the sonic log in $\mu$s/ft,

$t_{ma}$ is the transit time of the matrix material,

and

$t_f$ is the transit time of the saturating fluid (about 189 $\mu$s/ft for freshwater mud systems).

Generally, consolidated and compacted sandstones have porosities from 15 to 25%. In such formations, the response of the sonic log seems to be relatively independent of the exact contents of the pores: water, oil, gas, or even disseminated shale. However, in some higher porosity sandstones (30% or greater) that have very low water saturation (high hydrocarbon saturation) and very shallow invasion, the $t$ values may be somewhat greater than those in the same formations when water saturated.

If any shale laminae exist within the sandstone, the apparent sonic porosity values are usually increased by an amount proportional to the bulk volume fraction of laminae. The $t$ readings are increased because $t_{sh}$ is generally greater than $t_{ma}$ of the sandstone matrix.

Carbonates

In carbonates having intergranular porosity the time-average formula still applies, but, sometimes, pore structure and pore size distribution are quite different from that of sandstones. There is often some secondary porosity consisting of vugs and/or fractures with much larger dimensions than the pores of the primary porosity.

In vuggy formations, the velocity of sound seems to depend mostly on the primary intergranular porosity, and the porosity derived from the sonic reading through the time-average formula ($\phi_{SV}$) will tend to be too low by an amount approaching the secondary porosity. Thus, if the total porosity ($\phi_t$) of a formation exhibiting primary and secondary porosity ($\phi_2$) is available (from a neutron and/or density log, for example), the amount of secondary porosity can be estimated:

$$\phi_2 = \phi_t - \phi_{SV}. \qquad \text{(Eq. 5-2)}$$

Uncompacted Sands

Direct application of the time-average equation gives values of porosity that are too high in unconsolidated and insufficiently compacted sands. Uncompacted sands are most prevalent in the geologically younger formations, particularly at shallow depths. However, even at deeper depths these younger sands are often uncompacted when the overburden-to-formation fluid pressure differentials are less than about 4000 to 5000 psi. Such lack of compaction may be indicated when adjacent shales exhibit $t$ values greater than 100 $\mu$s/ft.

When the formations are not sufficiently compacted, the observed $t$ values are greater than those that correspond to the porosity according to the time-average formula, but the $\phi$ versus $t$ relationship is still approximately linear. In these cases, an empirical correction factor, $C_p$, is applied to Eq. 5-1 to give a corrected porosity, $\phi_{SVcor}$:

$$\phi_{SVcor} = \frac{t - t_{ma}}{t_f - t_{ma}} \cdot \frac{1}{C_p}. \qquad \text{(Eq. 5-3)}$$

The value of $C_p$ is given approximately by dividing the sonic velocity in nearby shale beds by 100. However, the compaction correction factor is best determined by comparing $\phi_{SV}$, as obtained from Eq. 5-1, with the true porosity obtained from another source. Several approaches are possible.

The $R_0$ method: Compare the sonic and induction or laterolog values in a clean water sand. The value of $R_0$ found from the resistivity is divided by $R_w$ to obtain $F$. Then $\phi$ is found from $F$ (Chart Por-2) and compared with $\phi_{SV}$ from Eq. 5-1 (sonic porosity without compaction correction). The value of $C_p$ is equal to $\phi_{SV}/\phi$. This value of $C_p$ can then be used to analyze nearby potential hydrocarbon-bearing sands.

Density-sonic crossplot method: When sonic and density logs are available, $\varrho_b$ (in ordinate) and $t$ (in abscissae) values are crossplotted over several sands in the interval of interest. If the sands contain no gas and some of them are clean, a line drawn from the matrix point through the points lying toward the upper left will be the clean sand line (Fig. 5-9). For any given porosity value on this clean sand line, there will be a value of $t$. Enter this $t$ in Chart Por-3 and go vertically to the $\phi$ value. The intersection will give the value for $C_p$. If a sand is known to be clean and liquid filled, then $C_p = \phi_{SV}/\phi_D$.

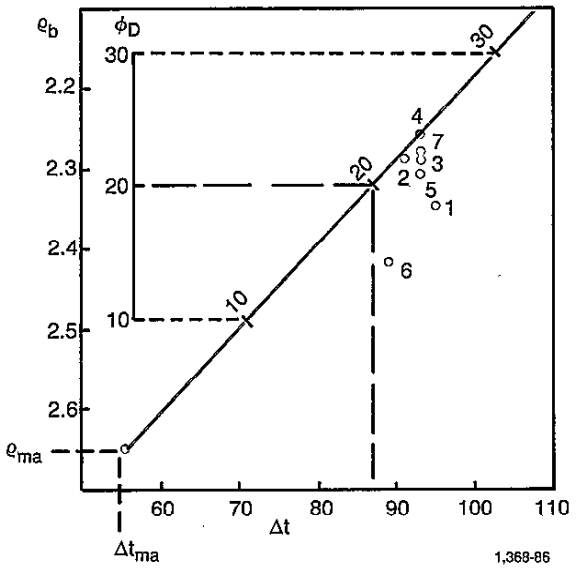


Fig. 5-9—Density-sonic crossplot as used for compaction-factor determination.

Neutron method: The previous two methods require a clean sand. If the sands are shaly, neither method can be safely used. If an SNP or CNL* neutron log is available, $\phi_N$ may be compared with $\phi_{SV}$ (or $t$) using Chart Por-3. Differences between $\phi_N$ and $\phi_{SV}$ in water-filled sands are due to lack of compaction. For such sands, $C_p = \phi_{SV}/\phi_N$.

In some shallowly invaded high-porosity rocks with high hydrocarbon saturation, sonic-derived porosity may be too high because of fluid effect. Both oil and gas transmit sound at lower velocities (higher transit times) than does water. Therefore, the transit time-to-porosity transform, which assumes water as the saturating pore fluid, sometimes overstates rock porosity. In these cases, the time average-derived porosity is multiplied by 0.9 in oil-bearing formations and by 0.7 in gas-bearing forma-

tions. These fluid corrections are applied only when the time average-derived porosity is obviously too high.

Empirical Equation Based on Field Observations

The long-standing problems with using the time-average equation, coupled with numerous comparisons of sonic transit time versus porosity, led to the proposal of an empirical transit time-to-porosity transform. The transform is also shown in Chart Por-3. The transform is empirical, being based entirely on comparisons of sonic transit time versus an independent porosity measurement.

The empirical transform exhibits several salient features. First, it appears that all pure quartz sandstones may be characterized by a unique matrix velocity, slightly less than 18,000 ft/sec. A value of 17,850 ft/sec (or $t_{ma}$ = 56 μs/ft) is suggested. Limestone and dolomite also seem to exhibit unique matrix velocities: 20,500 ft/sec (or $t_{ma}$ = 49 μs/ft) for limestone, and 22,750 ft/sec (or $t_{ma}$ = 44 μs/ft) for dolomite.

In sandstone, the transform yields slightly greater porosity values over the low- to medium-porosity range (i.e., the 5 to 25% range) than does the time-average equation using an 18,000 ft/sec matrix velocity. In fact, at 15% porosity the transform indicates a porosity similar to that given by the time-average equation using a matrix velocity of 19,500 ft/sec. Thus, it appears the higher matrix velocities used in sonic interpretation in the past have been selected to force the time-average equation to yield a truer porosity over the low to medium range; this is true for both carbonates and sandstones.

For moderately high porosity sands (30%), the proposed empirical transform generally corresponds to the time-average equation using $v_{ma}$ = 18,000 ft/sec. Above 35% porosity, however, sonic transit time increases much more rapidly than porosity, and its response quickly departs from that predicted by the time-average equation. This is the region in which the time-average equation would require a "lack of compaction" correction. The new transform eliminates the need for the correction factor and yields porosity directly.

This empirical transform can be approximated over the range of normally encountered porosities by the following equation:

$$\phi_{SV} = C \frac{(t_{LOG} - t_{ma})}{t_{LOG}}. \quad \text{(Eq. 5-4)}$$

The value of the constant $C$ has a range of 0.625 to 0.7 depending upon the investigator. Chart Por-3 uses 0.7 for $C$: this was the value originally proposed. However, more recent transit time-to-porosity comparisons indicate 0.67 is more appropriate.

For the case of a gas-saturated reservoir rock, $C$ becomes 0.6. It should be used when the rock investigated by the sonic tool contains an appreciable amount of hydrocarbon in the gassy (vapor) phase. Because of the very shallow depth of investigation, this condition normally exists only in higher porosity sandstones (greater than 30%).

**Correlations with $t$ Curve**

Variations of velocity in different types of rock produce a sonic surve with a correlatable character. In addition, the very good vertical definition of the sonic log and the reduced hole effect because of borehole compensation make this log excellent for correlation. It is very helpful in some cases where other logs give poor results (thick shale sections and evaporites). Moreover, some types of formations, evaporites in particular, can be easily identified from their $t$ values.

**Abnormal Formation Pressures**

Formations having abnormally high fluid pressures are often overlain by overpressured shales, which have an excess of pore water. Sonic transit time is greater in these shales than in normally compacted shales. Thus, a sonic log may be used to predict the possibility of overpressure.

The sonic travel time in shales normally decreases with increasing burial depth. A plot of this trend, $t_{sh}$ versus depth, defines the normal compaction. Departures from this trend toward higher values suggest an abnormal, overpressured section (Fig. 5-10). With experience in the area, the magnitude of the overpressure can often be related to the difference between the actual shale transit time and that expected from the normal compaction trend line.

**Shear-Wave Interpretation**

All the preceding discussion has concerned compressional transit time interpretation. With the Array-Sonic tool and full-waveform recording, it is now possible to obtain shear-wave transit time measurements on a more routine basis. Application of the shear wave in formation evaluation is only now beginning to be explored. It is obvious that shear-wave velocity data will be useful in calculating rock elastic or inelastic properties and as an adjunct to shear seismic data.

Shear-wave transit time data are also useful in identifying matrix minerals and pore fluids (Fig. 5-11). For example, a crossplot of compressional transit time, $t_c$, and shear transit time, $t_s$, can be used to identify the mineral content of the various rocks traversed by the wellbore. The technique is similar to other porosity log crossplotting techniques (e.g., density-neutron, sonic-density, sonci-neutron).

There is evidence that the shear-wave transit time may be useful for fluid identification. Laboratory observations

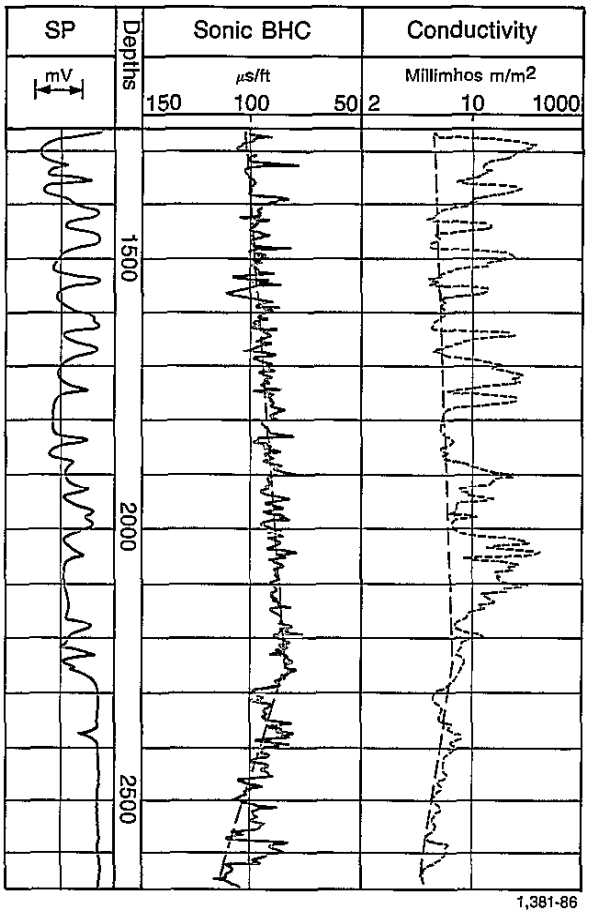


Fig. 5-10—Detecting overpressured zone with the sonic log.

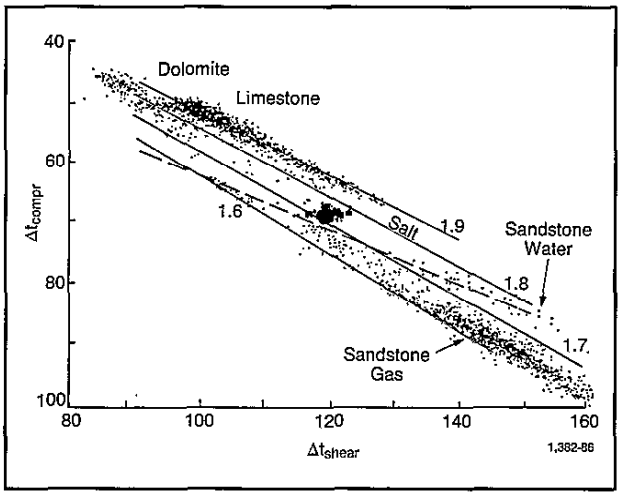


Fig. 5-11—$\Delta t_{compr}$—$\Delta t_{shear}$ crossplots.

suggest that light hydrocarbon saturation decreases the velocity of the compressional wave (relative to brine saturation) through the porous rock and increases the velocity of the shear wave.

A relationship between porosity and shear velocity (or interval transit time) has also been noted. Indeed, the time-average relationship (Eq. 5-1) and the empirical relationship (Eq. 5-4) that relate compressional transit time to porosity appear to apply to shear transit time as well. Of course, appropriate matrix and fluid parameters must be used. For shear-wave propagation, the parameters are approximately:

| | | | |
|---|---|---|---|
| Sandstone, | $t_{ma}$ | ≈ | 86 μs/ft |
| Limestone, | $t_{ma}$ | ≈ | 90 μs/ft |
| Dolomite, | $t_{ma}$ | ≈ | 76 μs/ft |
| Anhydrite, | $t_{ma}$ | ≈ | 100 μs/ft |
| Water, | $t_{ma}$ | ≈ | 350 μ/ft |

These values are tentative. Further experience with the shear transit time may lead to some refinement. Also, the listing of a shear transit time value for water is somewhat imaginary since water does not support shear-wave propagation. However, the use of the listed value for water in the time-average equation does seem to yield acceptable porosity values.

## DENSITY LOGS

Density logs are primarily used as porosity logs. Other uses include identification of minerals in evaporite deposits, detection of gas, determination of hydrocarbon density, evaluation of shaly sands and complex lithologies, determinations of oil-shale yield, calculation of overburden pressure and rock mechanical properties.

### Principle

A radioactive source, applied to the borehole wall in a shielded sidewall skid, emits medium-energy gamma rays into the formations. These gamma rays may be thought of as high-velocity particles that collide with the electrons in the formation. At each collision a gamma ray loses some, but not all, of its energy to the electron, and then continues with diminished energy. This type of interaction is known as Compton scattering. The scattered gamma rays reaching the detector, at a fixed distance from the source, are counted as an indication of formation density.

The number of Compton-scattering collisions is related directly to the number of electrons in the formation. Consequently, the response of the density tool is determined essentially by the electron density (number of electrons per cubic centimeter) of the formation. Electron density is related to the true bulk density, $\varrho_b$, which, in turn,

depends on the density of the rock matrix material, the formation porosity, and the density of the fluids filling the pores.

### Equipment

To minimize the influence of the mud column, the skid-mounted source and detector are shielded. The openings of the shields are applied against the wall of the borehole by an eccentering arm. The force exerted by the arm, and the plow-shaped design of the skid, allow it to cut through soft mudcakes. Any mudcake or mud remaining between the tool and the formation is "seen" as part of the formation and must be accounted for.

A correction is needed when the contact between the skid and the formations is not perfect (mudcake or irregularities in the borehole wall). In unfavorable cases this correction can be fairly large. If only one detector is used, the correction is not easy to determine because it depends on the thickness, the weight, and even the composition of the mudcake or mud interposed between the skid and the formations.

In the FDC* compensated formation density tool, two detectors of differing spacing and depth of investigation are used, as shown on Fig. 5-12. The chart of Fig. 5-13 is a plot of long-spacing versus short-spacing count rates. Points for a given value of $\varrho_b$ and various mudcake conditions fall on or very close to an average curve. Using these average curves it is possible to enter the chart with the two count rates and determine the corrected $\varrho_b$ from the plot without any explicit measurement of mudcake density or thickness. This measurement technique is referred to as "spine and ribs."

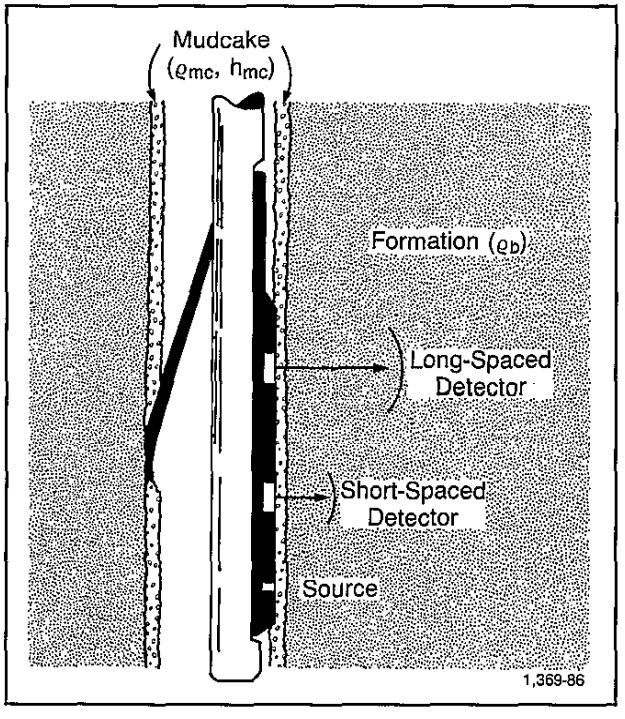


Fig. 5-12—Schematic drawing of the dual spacing Formation Density Logging Device (FDC). (Ref. 16)

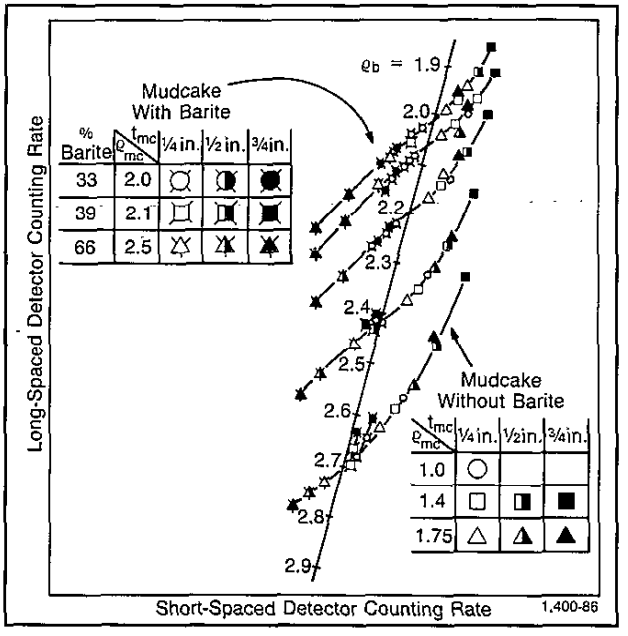


Fig. 5-13—"Spine-and-ribs" plot, showing response of FDC counting rates to mudcake. (Ref. 16)

The correction is made automatically and the corrected $\varrho_b$ curve and $\Delta\varrho$ (the correction made) are recorded directly on the log (Fig. 5-14).

The distance between the face of the skid and the extremity of the eccentering arm is recorded as a caliper log, which helps to assess the quality of contact between the skid and the formation.

### Logging Empty Holes

The spine-and-ribs plot for empty holes is not the same as that shown in Fig. 5-13. When the density tool is used in empty hole, the bulk density is automatically computed according to the empty-hole tool response.

### Log Presentation

Log information is presented as shown in Fig. 5-14. The bulk density curve, $\varrho_b$, is recorded in Tracks 2 and 3 with a linear density scale in grams per cubic centimeter. An optional porosity curve may also be recorded in Tracks 2 and 3. This is a continuous solution of Eq. 5-7, using preset values of $\varrho_{ma}$ and $\varrho_f$ selected according to conditions. The $\Delta\varrho$ (which shows how much density compensation has been applied to correct for mudcake and hole rugosity) is usually recorded in Track 3. The caliper is

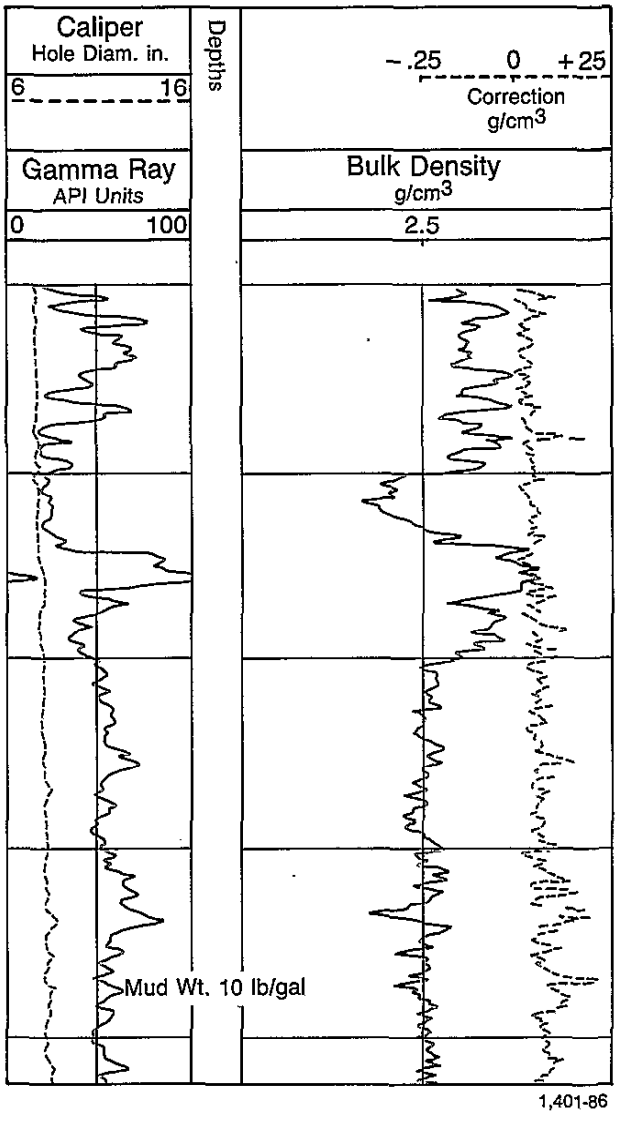


Fig. 5-14—FDC log presentation. (Ref. 16)

recorded in Track 1. A gamma ray (GR) curve may also be simultaneously recorded in Track 1. If a CNL* compensated neutron log is run in combination with the FDC log, it is also recorded in Tracks 2 and 3.

### Calibration

The primary calibration standards for the FDC tool are laboratory freshwater-filled limestone formations of high purity and known densities. The secondary (shop calibration) standards are large aluminum and sulfur blocks into which the sonde is inserted. These blocks are of carefully designed geometry and composition, and their characteristics have been related to the limestone formations. With the blocks, two different thicknesses of artificial mudcakes are used to check the automatic mudcake correction. Finally, at the wellsite, a radioactive test jig is used to produce a signal of known intensity to verify the detection system.

### Borehole Effect

Chart Por-15 shows the corrections needed for borehole sizes up to 15 in. in mud- and gas-filled boreholes. The corrections are negligible for holes smaller than 10 in. in diameter.

The FDC tool may not always follow the same track up the side of the hole on subsequent — overlap and/or repeat — runs. If the formations are quite heterogeneous—having, for instance, more vugs and/or fissures on one side of the hole wall than on the other—the two runs may disagree slightly. Disagreement is infrequently encountered, however, because the heavy skid tends to ride the downhill side of the hole, which seldom is absolutely vertical.

### Electron Density and Bulk Density

The density log responds to the electron density of the formations. For a substance consisting of a single element, the electron density index, $\varrho_e$, is related to the bulk density, $\varrho_b$ :

$$\varrho_e = \varrho_b \left(\frac{2Z}{A}\right), \qquad \text{(Eq. 5-5a)}$$

where

$\varrho_b$ is the actual bulk density,

$Z$ is the atomic number (number of electrons per atom),

and

$A$ is the atomic weight ($\varrho_b/A$ is proportional to the number of atoms per cubic centimeter of the substance).

For a molecular substance, the electron density index is related to the bulk density:

$$\varrho_e = \varrho_b \quad 2 \left(\frac{\Sigma Z\text{'s}}{\text{Mol. Wt.}}\right), \qquad \text{(Eq. 5-5b)}$$

where

$\Sigma Z$'s is the sum of the atomic numbers of atoms making up the molecule (equal to the number of electrons per molecule) and Mol. Wt. is the molecular weight.

For most formation substances, the bracketed quantities in Eqs. 5-5a and 5-5b are very close to unity (Column 4 of Tables 5-2 and 5-3). When the density tool is calibrated in freshwater-filled limestone formations, the apparent bulk density, $\varrho_a$, as read by the tool is related to the electron density index, $\varrho_e$, by:

$$\varrho_a = 1.0704\ \varrho_e - 0.1883. \qquad \text{(Eq. 5-6)}$$

**Table 5-2**

| Element | A | Z | $2\frac{Z}{A}$ |
|---|---|---|---|
| H | 1.008 | 1 | 1.9841 |
| C | 12.011 | 6 | 0.9991 |
| O | 16.000 | 8 | 1.0000 |
| Na | 22.990 | 11 | 0.9569 |
| Mg | 24.320 | 12 | 0.9868 |
| Al | 26.980 | 13 | 0.9637 |
| Si | 28.090 | 14 | 0.9968 |
| S | 32.070 | 16 | 0.9978 |
| Cl | 35.460 | 17 | 0.9588 |
| K | 39.100 | 19 | 0.9719 |
| Ca | 40.080 | 20 | 0.9980 |

1,386-86

For liquid-filled sandstones, limestones, and dolomites the tool reading, $\varrho_a$, is practically identical to actual bulk density, $\varrho_b$. For a few substances, such as sylvite, rock salt, gypsum, anhydrite, coal, and gas-bearing formations, the corrections shown in Fig. 5-15 are needed to obtain bulk density values from the density log readings.

**Porosity From Density Log**

For a clean formation of known matrix density, $\varrho_{ma}$, having a porosity, $\phi$, that contains a fluid of average density, $\varrho_f$, the formation bulk density, $\varrho_b$, will be:

$$\varrho_b = \phi\, \varrho_f + (1 - \phi)\, \varrho_{ma}\,. \qquad \text{(Eq. 5-7a)}$$

For usual pore fluids (excepting gas and light hydrocarbons) and for common reservoir matrix minerals, the difference between the apparent density $\varrho_a$, read by the density log, and the bulk density, $\varrho_b$, is so trivial that it is disregarded. Solving for $\phi$,

$$\phi = \frac{\varrho_{ma} - \varrho_b}{\varrho_{ma} - \varrho_f}, \qquad \text{(Eq. 5-7b)}$$

where $\varrho_b = \varrho_a$ (with exceptions noted).

Common values of $\varrho_{ma}$ are given in Table 5-3.

The fluid in the pores of the permeable formations, within the relatively shallow zone investigated by the tool (about 6 in.), is usually mostly mud filtrate. This mud filtrate may have a density ranging from slightly less than 1 to more than 1.1 depending upon its salinity, temperature, and pressure. Fig. 5-16 shows the densities

**Table 5-3**

| Compound | Formula | Actual Density $\varrho_b$ | $\frac{2\Sigma Z's}{\text{Mol. Wt.}}$ | $\varrho_e$ | $\varrho_a$ (as seen by tool) |
|---|---|---|---|---|---|
| Quartz | $SiO_2$ | 2.654 | 0.9985 | 2.650 | 2.648 |
| Calcite | $CaCO_3$ | 2.710 | 0.9991 | 2.708 | 2.710 |
| Dolomite | $CaCO_3MgCO_3$ | 2.850 | 0.9977 | 2.863 | 2.850 |
| Anhydrite | $CaSO_4$ | 2.960 | 0.9990 | 2.957 | 2.977 |
| Sylvite | KCl | 1.984 | 0.9657 | 1.916 | 1.863 |
| Halite | NaCl | 2.165 | 0.9581 | 2.074 | 2.032 |
| Gypsum | $CaSO_4 2H_2O$ | 2.320 | 1.0222 | 2.372 | 2.351 |
| Anthracite Coal | | {1.400 / 1.800} | 1.0300 | {1.442 / 1.852} | {1.355 / 1.796} |
| Bituminous Coal | | {1.200 / 1.500} | 1.0600 | {1.272 / 1.590} | {1.173 / 1.514} |
| Fresh Water | $H_2O$ | 1.000 | 1.1101 | 1.110 | 1.000 |
| Salt Water | 200,000 ppm | 1.146 | 1.0797 | 1.237 | 1.135 |
| Oil | $n(CH_2)$ | 0.850 | 1.1407 | 0.970 | 0.850 |
| Methane | $CH_4$ | $\varrho_{meth}$ | 1.2470 | 1.247 $\varrho_{meth}$ | 1.335 $\varrho_{meth}$—0.188 |
| Gas | $C_{1.1}H_{4.2}$ | $\varrho_g$ | 1.238 | 1.238 $\varrho_g$ | 1.325 $\varrho_g$—0.188 |

1,387-86

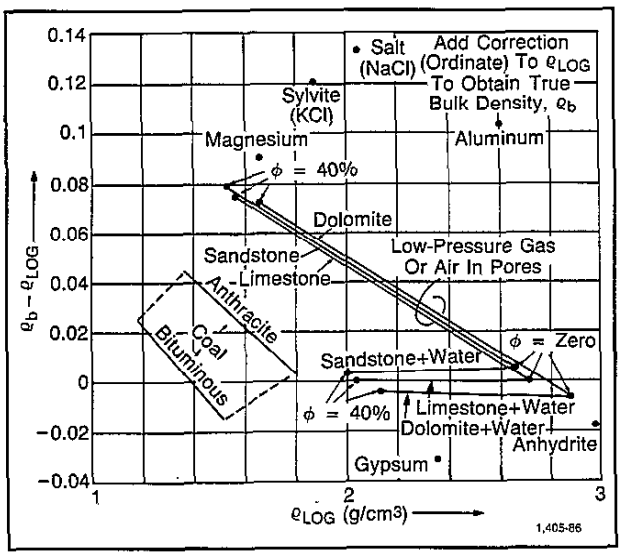


Fig. 5-15—Correction needed to get true bulk density from log density. (Ref. 2)

of water and NaCl solutions at various temperatures, pressures, and salinities. At 75° F and atmospheric pressure, the relation between NaCl water salinity and density may be approximated by

$$\varrho_w = 1 + 0.73\ P, \qquad \text{(Eq. 5-8)}$$

where $P$ is the NaCl concentration in ppm $\times\ 10^{-6}$.

Chart Por-5 shows FDC porosities versus $\varrho_b$ readings for various matrices and $\varrho_f$ values of 1 through 1.2.

### Effect of Hydrocarbons

If residual hydrocarbons exist in the region investigated by the FDC tool, their presence may affect the log readings. The effect of oil may not be noticeable because the average fluid density, $\varrho_f$, (from $\varrho_o$ and $\varrho_{mf}$) will probably still be close to unity. If there is appreciable residual gas saturation, its effect will be to lower the $\varrho_a$.

Fig. 5-15 shows the corrections that must be added to the recorded $\varrho_a$ values to obtain true $\varrho_b$ values when low-pressure gas or air ($\varrho_g \approx 0$) occupies the pores.

The apparent density of gas, as seen by the density log, can be computed if the composition and density of the gas are known. Fig. 5-17 is a chart showing, for a gas of specified composition, the values of $\varrho_g$ (actual density) and $\varrho_{ga}$, the apparent gas density seen by the density tool (based on electron density) as a function of pressure and temperature. In formations saturated with gas in the vicinity of the borehole, use $\varrho_{ga}$ instead of $\varrho_f$ in Eq. 3-7.

### Effect of Shale

Interpretation can be affected by shale or clay in the formations. Although the properties of shales vary with the

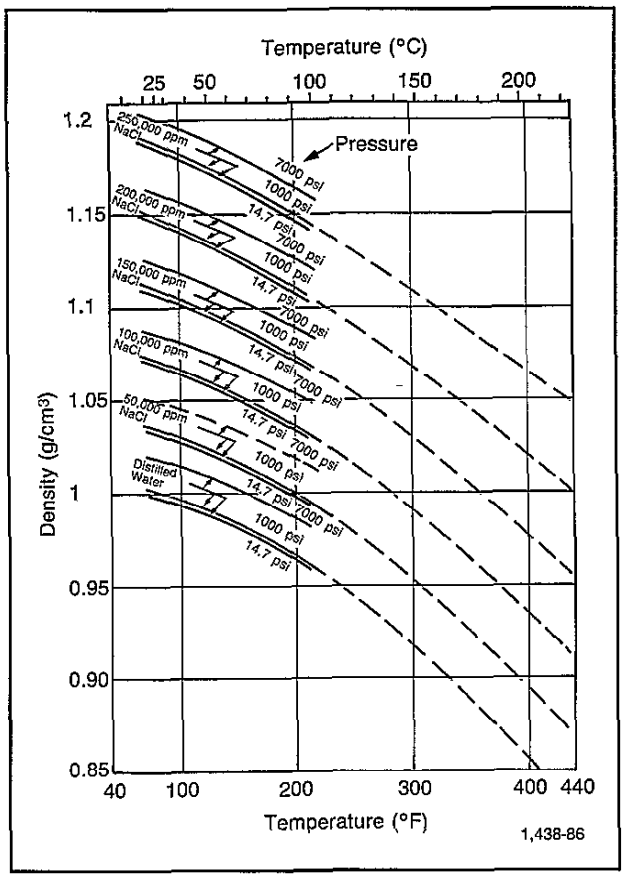


Fig. 5-16—Densities of water and NaCl solutions at varying temperatures and pressures.

formation and locality, typical densities for shale beds and laminar shale streaks are of the order of 2.2 to 2.65 g/cm$^3$. Shale densities tend to be lower at shallow depths where compacting forces are not as great. Dispersed clay or shale disseminated in the pore spaces may have a somewhat lower density than the interbedded shales.

### Effect of Pressure

The bulk density of shale increases with compaction, and in areas where the sediments are relatively young the increase of shale density with depth is apparent on the logs. However, departure from this trend is observed in overpressured zones; shale density decreases with increasing depth (Fig. 5-18). This decrease often appears in shales as much as several hundred feet above high-pressure permeable sands. A high-density zone (the sealing barrier) usually lies at the top of this interval of decreased density. Density logs run at intervals during the drilling of a well can be used to predict abnormally pressured zones so that precautions can be taken to eliminate possible hazards.

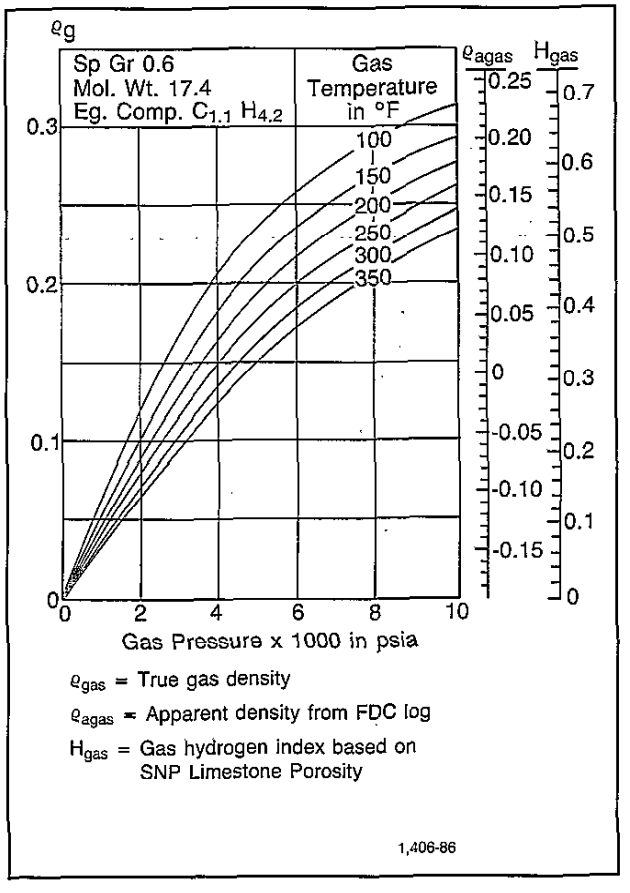


Fig. 5-17—Gas density and hydrogen index as functions of pressure and temperature for a gas mixture slightly heavier than methane ($C_{1.1}$ $H_{4.2}$).

### Litho-Density* Log

The Litho-Density log is an improved and expanded version of the FDC log. In addition to the bulk density measurement, the tool also measures the photoelectric absorption index of the formation, $P_e$. Photoelectric absorption can be related to lithology; whereas the $\varrho_b$ measurement responds primarily to porosity and secondarily to rock matrix and pore fluid, the $P_e$ measurement responds primarily to rock matrix (lithology) and secondarily to porosity and pore fluid.

#### Equipment

In appearance and operation, the Litho-Density tool is similar to the FDC tool. The tool has a pad, or skid, in which the gamma ray source and two detectors are located. This skid is held against the borehole wall by a spring-activated backup arm. Gamma rays, emitted by the source at an energy of 662 keV, are scattered by the formation and lose energy until absorbed through photoelectric effect.

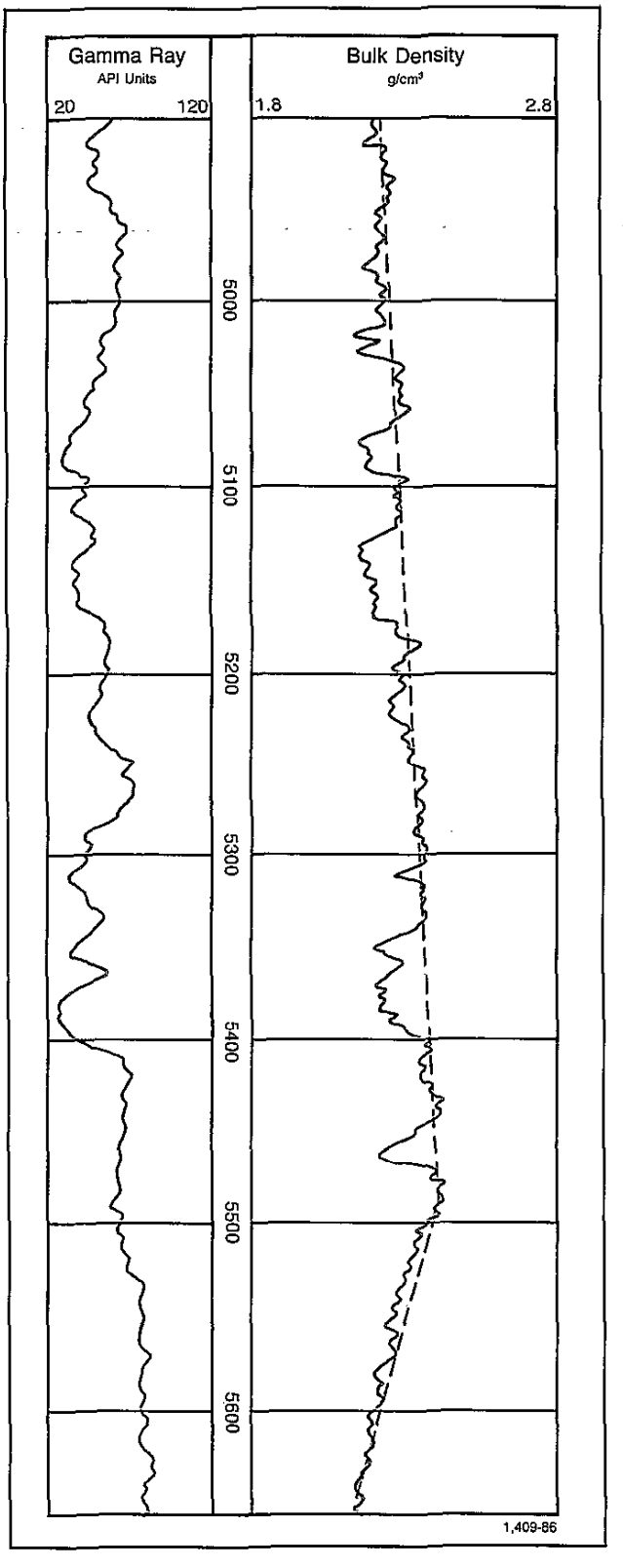


Fig. 5-18—Density log in overpressured shales.

At a finite distance from the source, such as the far detector, the energy spectrum might look as illustrated in Fig. 5-19. The number of gamma rays in the higher energy region (region of Compton scattering) is inversely related only to the electron density of the formation (i.e., an increase in the formation density decreases the number of gamma rays). The number of gamma rays in the lower energy region (region of photoelectric effect) is inversely related to both the electron density and the photoelectric absorption. By comparing the counts in these two regions, the photoelectric absorption index can be determined.

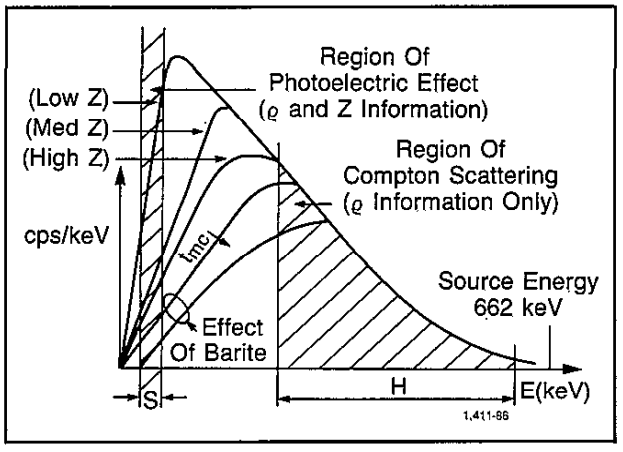


Fig. 5-19—Variations in spectrum for formation with constant density but different $Z$.

The gamma ray spectrum at the near detector is used only to correct the density measurement from the far detector for the effects of mudcake and borehole rugosity.

## Photoelectric Absorption

In nuclear experiments, cross section is defined as a measure of the probability that a nuclear reaction will take place, under specified conditions, between two particles or a particle and another target. It is usually expressed in terms of the effective area a single target presents to the incoming particle. Table 5-4 lists the photoelectric absorption cross section, given in barns per atom, for several elements at the incident gamma ray energy level. The atomic number, $Z$, for each of these elements is also listed. The photoelectric cross section index, $P_e$, in barns per electron is related to $Z$ by:

$$P_e = \left(\frac{Z^{3.6}}{10}\right). \qquad \text{(Eq. 5-9)}$$

**Table 5-4**

| Element | Photoelectric Cross Section | Atomic Number $Z_e$ |
|---|---|---|
| Hydrogen | 0.00025 | 1 |
| Carbon | 0.15898 | 6 |
| Oxygen | 0.44784 | 8 |
| Sodium | 1.4093 | 11 |
| Magnesium | 1.9277 | 12 |
| Aluminum | 2.5715 | 13 |
| Silicon | 3.3579 | 14 |
| Sulfur | 5.4304 | 16 |
| Chlorine | 6.7549 | 17 |
| Potassium | 10.0810 | 19 |
| Calcium | 12.1260 | 20 |
| Titanium | 17.0890 | 22 |
| Iron | 31.1860 | 26 |
| Copper | 46.2000 | 29 |
| Strontium | 122.2400 | 38 |
| Zirconium | 147.0300 | 40 |
| Barium | 493.7200 | 56 |

1,388-86

For a molecule made up of several atoms, a photoelectric absorption cross section index, $P_e$, may be determined based upon atomic fractions. Thus,

$$P_e = \frac{\Sigma\, A_i\, Z_i\, P_i}{\Sigma\, A_i\, Z_i}, \qquad \text{(Eq. 5-10)}$$

where $A_i$ is the number of each atom in the molecule.

Table 5-5 gives the $P_e$ value for several reservoir rocks, minerals, and fluids commonly encountered in the oil field. From this list it is not readily apparent that the cross section is relatively independent of porosity and the saturating fluid. To verify this relative independence, express the photoelectric absorption cross section index in volumetric terms rather than in electron terms.

By definition:

$$U = P_e\, \varrho_e.$$

Since $P_e$ has the units of barns per electron and $\varrho_e$ the units of electrons per cubic centimeter, $U$ has the units of barns per cubic centimeter. This parameter permits the cross sections of the various volumetric components of a formation to be added in a simple weighted average manner. Thus,

$$U = \phi\, U_f + (1 - \phi)\, U_{ma}, \qquad \text{(Eq. 5-11)}$$

where $U$, $U_f$, and $U_{ma}$ are the photoelectric absorption cross sections of the mixture, pore fluid, and matrix, respectively; all are expressed in barns per cubic centimeter. Transformation of the mixture response given by Eq. 5-11 back into $P_e$ gives the response shown in Chart CP-16 when $P_e$ is crossplotted against bulk density.

**Table 5-5**

| Name | Formula | Molecular Weight | $P_e$ | $\varrho_b$ | $\varrho_a$ | U |
|---|---|---|---|---|---|---|
| **Minerals** | | | | | | |
| Anhydrite | $CaSO_3$ | 136.146 | 5.055 | 2.960 | 2.957 | 14.95 |
| Barite | $BaSO_4$ | 233.366 | 266.800 | 4.500 | 4.011 | 1070.00 |
| Calcite | $CaCO_3$ | 100.090 | 5.084 | 2.710 | 2.708 | 13.77 |
| Carnallite | $KCl\text{-}MgCl_2\text{-}6H_2O$ | 277.880 | 4.089 | 1.610 | 1.645 | 6.73 |
| Celestite | $SrSO_4$ | 183.696 | 55.130 | 3.960 | 3.708 | 204.00 |
| Corundum | $Al_2O_3$ | 101.900 | 1.552 | 3.970 | 3.894 | 6.04 |
| Dolomite | $CaCO_3M_gCO_3$ | 184.420 | 3.142 | 2.850 | 2.864 | 9.00 |
| Gypsum | $CaSO_4\text{-}2H_2O$ | 172.180 | 3.420 | 2.320 | 2.372 | 8.11 |
| Halite | NaCl | 58.450 | 4.650 | 2.165 | 2.074 | 9.65 |
| Hematite | $Fe_2O_3$ | 159.700 | 21.480 | 5.210 | 4.987 | 107.00 |
| Ilmenite | $FeO\text{-}TiO_2$ | 151.750 | 16.630 | 4.700 | 4.460 | 74.20 |
| Magnesite | $MgCO_3$ | 84.330 | 0.829 | 3.037 | 3.025 | 2.51 |
| Magnetite | $Fe_3O_4$ | 231.550 | 22.080 | 5.180 | 4.922 | 109.00 |
| Marcasite | $FeS_2$ | 119.980 | 16.970 | 4.870 | 4.708 | 79.90 |
| Pyrite | $FeS_2$ | 119.980 | 16.970 | 5.000 | 4.834 | 82.00 |
| Quartz | $SiO_2$ | 60.090 | 1.806 | 2.654 | 2.650 | 4.79 |
| Rutile | $TiO_2$ | 79.900 | 10.080 | 4.260 | 4.052 | 40.80 |
| Sylvite | KCl | 74.557 | 8.510 | 1.984 | 1.916 | 16.30 |
| Zircon | $ZrSiO_4$ | 183.310 | 69.100 | 4.560 | 4.279 | 296.00 |
| **Liquids** | | | | | | |
| Water | $H_2O$ | 18.016 | 0.358 | 1.000 | 1.110 | 0.40 |
| Salt Water | (120,000 ppm) | | 0.807 | 1.086 | 1.185 | 0.96 |
| Oil | $CH_{1.6}$ | | 0.119 | 0.850 | 0.948 | 0.11 |
| | $CH_2$ | | 0.125 | 0.850 | 0.970 | 0.12 |
| **Miscellaneous** | | | | | | |
| Clean Sandstone | | | 1.745 | 2.308 | 2.330 | 4.07 |
| Dirty Sandstone | | | 2.700 | 2.394 | 2.414 | 6.52 |
| Average Shale | | | 3.420 | 2.650 | 2.645 | 9.05 |
| Anthracite | C:H:O – | | 0.161 | 1.700 | 1.749 | 0.28 |
| Coal | 93:3:4 | | | | | |
| Bituminous | C:H:O – | | 0.180 | 1.400 | 1.468 | 0.26 |
| Coal | 82:5:13 | | | | | |

1,390-86

Tool Response

The Litho-Density tool skid and detector system have been designed so that greater counting rates are obtained than with the FDC tool and result in lower statistical variations and better repeatability of the measurements. The geometry of the skid has also been altered so that the density reading has a greater vertical resolution than that of the FDC measurement. The $P_e$ measurement exhibits an even better vertical resolution; this has applications in identifying fractures and laminar formations.

The procedure for mudcake and borehole rugosity compensation with the Litho-Density tool uses "spine and rib" as done with the FDC tool. Because of the fixed radius of curvature of the measuring device surface, borehole size also influences the measurement. The borehole-size correction is shown in Chart Por-5.

## NEUTRON LOGS

Neutron logs are used principally for delineation of porous formations and determination of their porosity. They respond primarily to the amount of hydrogen in the formation. Thus, in clean formations whose pores are filled with water or oil, the neutron log reflects the amount of liquid-filled porosity.

Gas zones can often be identified by comparing the neutron log with another porosity log or a core analysis. A combination of the neutron log with one or more other porosity logs yields even more accurate porosity values and lithology identification—even an evaluation of shale content.

### Principle

Neutrons are electrically neutral particles, each having a mass almost identical to the mass of a hydrogen atom. High-energy (fast) neutrons are continuously emitted from a radioactive source in the sonde. These neutrons collide with nuclei of the formation materials in what may be thought of as elastic "billiard-ball" collisions. With each collision, the neutron loses some of its energy.

The amount of energy lost per collision depends on the relative mass of the nucleus with which the neutron collides. The greater energy loss occurs when the neutron strikes a nucleus of practically equal mass — i.e., a hydrogen nucleus. Collisions with heavy nuclei do not slow the neutron very much. Thus, the slowing of neutrons depends largely on the amount of hydrogen in the formation.

Within a few microseconds the neutrons have been slowed by successive collisions to thermal velocities, corresponding to energies of around 0.025 eV. They then diffuse randomly, without losing more energy, until they are captured by the nuclei of atoms such as chlorine, hydrogen, or silicon.

The capturing nucleus becomes intensely excited and emits a high-energy gamma ray of capture. Depending on the type of neutron tool, either these capture gamma rays or the neutrons themselves are counted by a detector in the sonde.

When the hydrogen concentration of the material surrounding the neutron source is large, most of the neutrons are slowed and captured within a short distance of the source. On the contrary, if the hydrogen concentration is small, the neutrons travel farther from the source before being captured. Accordingly, the counting rate at the detector increases for decreased hydrogen concentration, and vice versa.

### Equipment

Neutron logging tools include the GNT tool series (no longer in use), the SNP sidewall neutron porosity tool (in limited use), and the CNL tool series, which includes the CNL compensated neutron and the Dual-Energy Neutron Log (DNL*). The current tools use americium-beryllium (AmBe) sources to provide neutrons with initial energies of several million electron volts.

The GNT tools were nondirectional devices that employed a single detector sensitive to both high-energy capture gamma rays and thermal neutrons. They could be run in cased or uncased holes. Although the GNT tools responded primarily to porosity, their readings were greatly influenced by fluid salinity, temperature, pressure, borehole size, standoff, mudcake, mud weight, and, in cased holes, by the casing and cement.

In the SNP tool the neutron source and detector are mounted on a skid, which is applied to the borehole wall. The neutron detector is a proportional counter, shielded so that only neutrons having energies above about 0.4 eV (epithermal) are detected.

The SNP tool has several advantages over the GNT tools:

- Because it is a sidewall device, borehole effects are minimized.
- Epithermal neutrons are measured, which minimizes the perturbing effects of strong thermal neutron absorbers (such as chlorine and boron) in the formation waters and matrix.
- Most required corrections are performed automatically in the surface instrumentation.
- It provides a good measurement in empty holes.

The SNP equipment is designed for operation only in open holes, either liquid filled or empty. The minimum hole diameter in which the tool can be used is 5 in. A caliper curve is recorded simultaneously with the SNP neutron data.

The CNL tool is a mandrel-type tool especially designed for combination with any of several other tools to provide a simultaneous neutron log. The CNL tool is a dual-spacing, thermal neutron-detection instrument. The ratio of counting rates from the two detectors is processed by the surface equipment to produce a linearly scaled recording of neutron porosity index. A 16-curie source and longer source-to-detector spacings give the CNL tool a greater radial depth of investigation than that of the SNP tool. The effects of borehole parameters are greatly reduced by taking the ratio of two counting rates similarly affected by these perturbations. The CNL tool can be run in liquid-filled holes, either cased or uncased, but cannot be used in gas-filled holes.

Since thermal neutrons are measured in the CNL tool, the response is affected by elements having a high thermal neutron capture cross section. The tool is sensitive to shale in the formation since shales usually contain small amounts of boron and other rare earth elements having a particularly high thermal neutron capture cross section. If excessive, this effect can mask the tool response to gas in shaly formations.

To improve the response to gas and to enhance interpretation in the presence of thermal neutron absorbers, the DNL tool incorporates two epithermal neutron detectors in addition to the two thermal neutron detectors (Fig. 5-20). Two separate porosity measurements are obtained, one from each pair of detectors. In clean formations the measured porosities generally agree. In shaly formations containing a large number of thermal neutron absorbers, the porosity measured by the epithermal detectors reads lower and agrees more closely with density-derived porosity. A comparison of the two porosity measurements indicates the shale or clay content, or the formation fluid salinity.

At a given source-detector spacing, epithermal neutron count rate is approximately an order of magnitude less than that for thermal neutrons. Therefore, to have reasonable epithermal neutron count rates, the epithermal detectors have been placed nearer to the neutron source than the thermal neutron detectors. The thermal neutron-detector configuration duplicates that of the standard CNL tool.

Since the two pairs of detectors are placed at different spacings and neutrons are detected at different energy levels, the environmental effects can be expected to be significantly different on the two neutron measurements.

If the ratio processing used on the thermal neutron measurement is used for the epithermal measurement, the computed porosity is quite sensitive to borehole effects. As a result of a detailed study of detector response to many environmental variables, an epithermal neutron processing technique has been developed that uses individual detector count rates. The method, which is

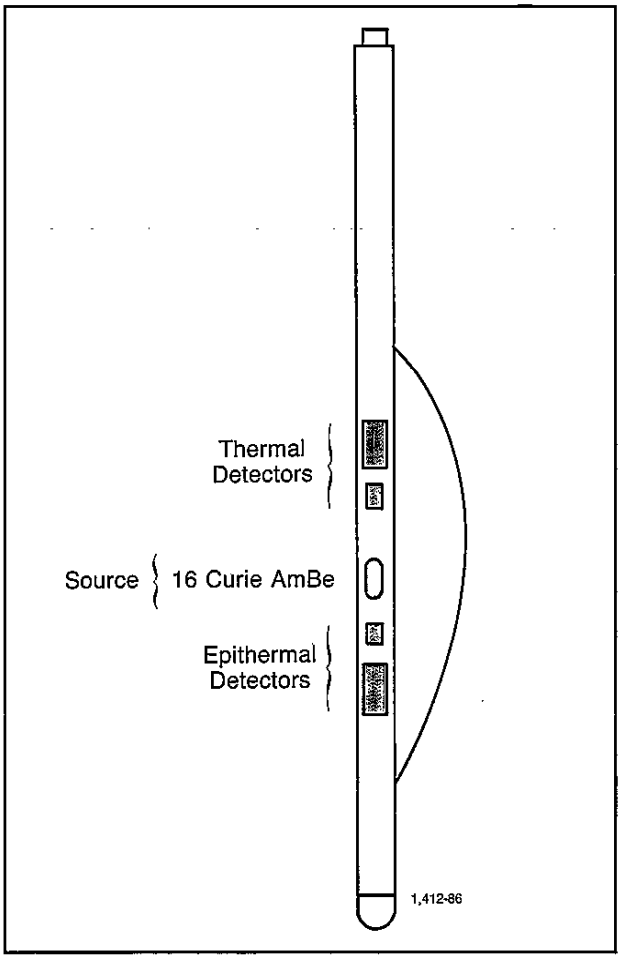


Fig. 5-20—DNL tool configuration, also known as CNT-G.

analogous to the spine-and-ribs analysis developed for the FDC tool, greatly reduces borehole effects on the epithermal neutron porosity measurement. The epithermal count rates can also be used to determine neutron porosity in air-filled boreholes.

The combined epithermal and thermal neutron Dual Porosity measurements provide improved porosity determination. Since the epithermal measurement is relatively free of neutron absorber effects, it yields improved gas detection in shaly reservoirs (Fig. 5-21). A comparison of the two neutron responses also provides information on the presence of materials with significant thermal neutron capture cross sections.

**Log Presentation**

SNP porosity readings are computed and recorded directly on the log (Fig. 5-22). The CSU* program automatically provides the corrections necessary in liquid-filled holes for mud weight, salinity, temperature, and hole-size variations. Chart Por-15 is used for mudcake correction. In

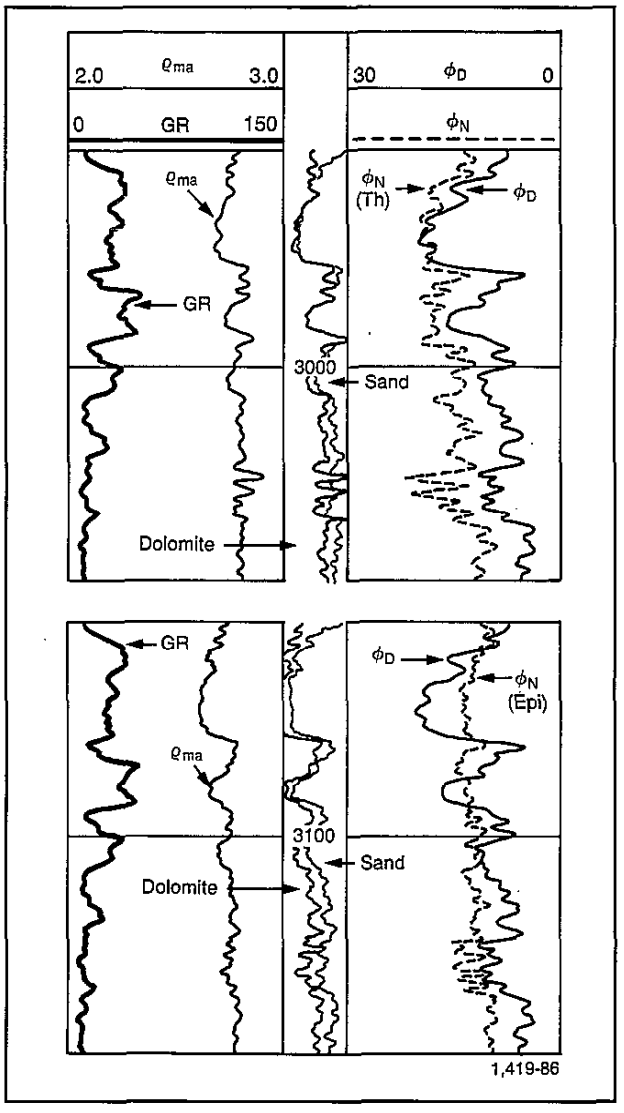


Fig. 5-21—Thermal/epithermal neutron log comparison in a gas zone.

gas-filled holes only the hole-size correction is required; it is done manually using a nomogram. The porosity values are recorded linearly in Tracks 2 and 3.

The CNL log and the DNL log are recorded in linear porosity units for a particular matrix lithology. When a CNL tool is run in combination with another porosity tool, all curves can be recorded on the same porosity scale. This overlay presentation permits visual qualitative interpretation of porosity and lithology or the presence of gas. Fig. 5-23 is an example of a combination CNL-FDC log.

### Calibration

The primary calibration standard for GNT neutron logs was the API neutron pit in Houston. The response of the

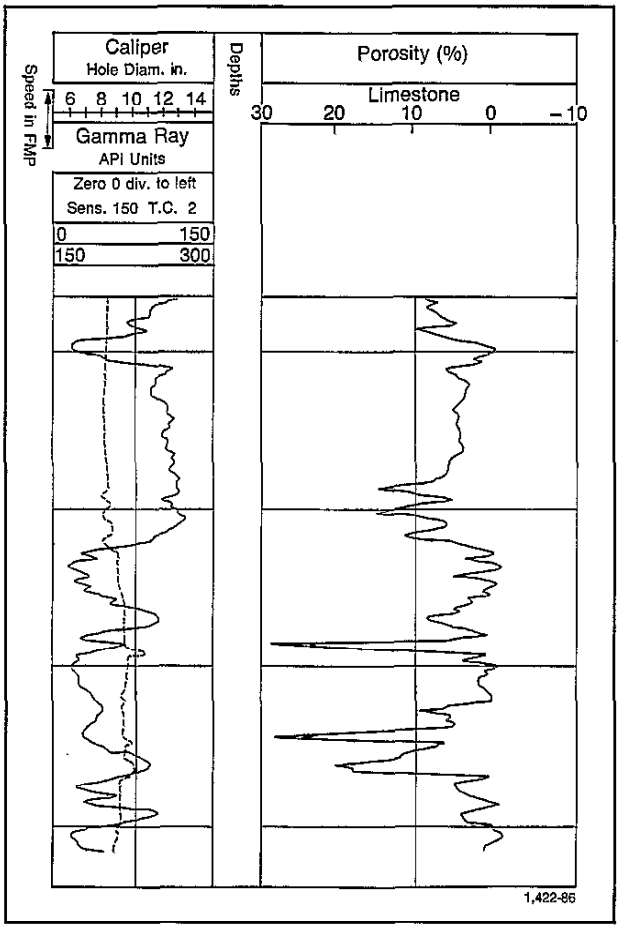


Fig. 5-22—Presentation of SNP log.

logging tool in a 19% porosity water-filled limestone was defined as 1,000 API units. Secondary calibrating devices, accurately related to the API pit, were used for the field calibration.

Prior to the API calibration procedure, neutron logs were scaled in counts per second. Conversion factors are provided in Table 5-6 to rescale them for comparison with neutron logs scaled in API units. Present neutron logs are scaled directly in porosity units.

**Table 5-6**

| Tool Type Source: PuBe or AmBe | Spacing in. | API Units per Std. CPS |
|---|---|---|
| GNT-F, G, H | 15.5 | 1.55 |
| GNT-F, H | 19.5 | 5.50 |
| GNT-G | 19.5 | 5.70 |
| GNT-J, K | 16 | 2.70 |

1,389-86

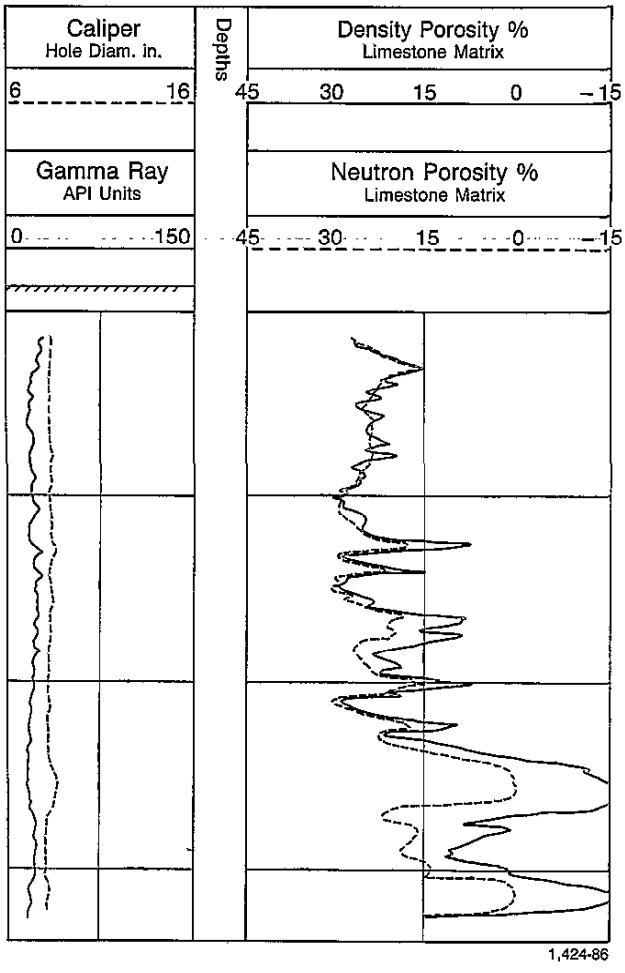


Fig. 5-23—Presentation of CNL-FDC log.

SNP tool calibration is based on numerous readings in formations of high purity and accurately known porosity. An environmental calibrator is used as a secondary standard at the wellsite. This device provides readings corresponding to 11% and 22% porosity in limestone.

The primary calibration standard for CNL tools is a series of water-filled laboratory formations. The porosities of these controlled formations are known within ± 0.5 porosity units. The secondary (shop) standard is a water-filled calibrating tank. A wellsite check is made by using a fixture that reproduces the count rate ratio obtained in the tank.

### Investigation Characteristics

The typical vertical resolution of the SNP and CNL tools is 2 ft. However, a new method of processing the count rates of the CNL tool is now available that increases the vertical resolution to 1 ft by exploiting the better vertical resolution of the near detector.

The radial investigation depends on the porosity of the formation. Very roughly, at zero porosity the depth of investigation is about 1 ft. At higher porosity in liquid-filled holes, the depth of investigation is less because neutrons are slowed and captured closer to the borehole. For average conditions, the depth of investigation for the SNP tool is about 8 in. in a high-porosity rock; it is about 10 in. for the CNL tool in similar conditions. Both tools sample a somewhat larger volume of formation than the FDC tools.

### Tool Response

As already stated, the responses of the neutron tools primarily reflect the amount of hydrogen in the formation. Since oil and water contain practically the same amount of hydrogen per unit volume, the responses reflect the liquid-filled porosity in clean formations. However, the tools respond to all the hydrogen atoms in the formation, including those chemically combined in formation matrix minerals.

Thus, the neutron reading depends mostly on the hydrogen index of the formation. The hydrogen index is proportional to the quantity of hydrogen per unit volume, with the hydrogen index of fresh water at surface conditions taken as unity.

### Hydrogen Index of Salt Water

Dissolved sodium chloride (NaCl) takes up space and thereby reduces the hydrogen density. An approximate formula for the hydrogen index of a saline solution at 75° F is

$$H_w = 1 - 0.4P, \qquad \text{(Eq. 5-12a)}$$

where $P$ is the NaCl concentration in ppm $\times 10^{-6}$. More generally, independent of temperatures,

$$H_w = \varrho_w (1 - P). \qquad \text{(Eq. 5-12b)}$$

In openhole logging, formations are generally invaded and the water in the zone investigated by the neutron logs is considered to have the same salinity as the borehole fluid. The SNP log is automatically corrected for salinity. The salinity correction to the CNL log is provided by Chart Por-14c.

For cased holes, the invaded zone usually disappears with time, and the water salinity is that of the formation water.

### Response to Hydrocarbons

Liquid hydrocarbons have hydrogen indexes close to that of water. Gas, however, usually has a considerably lower hydrogen concentration that varies with temperature and pressure. Therefore, when gas is present near enough to the borehole to be within the tool's zone of investigation,

a neutron log reads too low a porosity. This characteristic allows the neutron log to be used with other porosity logs to detect gas zones and identify gas/liquid contacts. A neutron and density log combination provides a more accurate porosity and a value of minimum gas saturation. (Hydrocarbon effect will be discussed further in Chapter 6 in the Crossplotting Section.)

The quantitative response of the neutron tool to gas or light hydrocarbon depends primarily on hydrogen index and another factor—the "excavation effect." The hydrogen index can be estimated from the composition and density of the hydrocarbon. For light hydrocarbons (gases), Fig. 5-15 provides an estimate of its hydrogen index, $H_h$. The hydrogen index of heavier hydrocarbons (oils) can be approximated by the equation:

$$H_o = 1.28\ \varrho_o. \qquad \text{(Eq. 5-13)}$$

This equation assumes the chemical composition of the oil is n $CH_2$. $H_o$ is derived from the comparison of the hydrogen density and molecular weight of water to those of oil.

Another set of equations can be used to estimate the hydrogen index of hydrocarbon fluids:

For light hydrocarbons ($\varrho_h < 0.25$),

$$H_h \approx 2.2\ \varrho_h. \qquad \text{(Eq. 5-14a)}$$

For heavy hydrocarbons ($\varrho_h > 0.25$),

$$H_h \approx \varrho_h + 0.3. \qquad \text{(Eq. 5-14b)}$$

Still another proposal suggests the equation

$$H_h = 9 \left(\frac{4 - 2.5\ \varrho_h}{16 - 2.5\ \varrho_h}\right) \varrho_h. \qquad \text{(Eq. 5-15)}$$

Mathematical investigations indicate that the effect of gas in the formation near the borehole is greater than would be expected by taking into account only its smaller hydrogen density. Previous calculations had been made as if the gas-filled portion of the porosity were replaced by rock matrix. The new calculations show that when this additional rock matrix is "excavated" and replaced with gas, the formation has a smaller neutron-slowing characteristic. The calculated difference in the neutron log readings has been termed the excavation effect. If this effect is ignored, too-high values of flushed-zone gas saturation and too-low values of porosity are given.

Fig. 5-24 shows the corrections needed for excavation effect. The values of porosity for sandstone, limestone, and dolomite lithologies are plotted. Intermediate porosity values can be interpolated.

The ordinate scale is used to correct neutron log porosities. An additional ordinate scale is provided for correcting porosities derived from a neutron-density crossplot that does not contain the excavation effect correction. Excavation effect corrections have already been incorporated into Chart CP-5.

The corrections for excavation effect given by Fig. 5-23 can be approximated by the formula

$$\Delta\phi_{Nex} = K\ [2\ \phi^2\ S_{wH} + 0.04\ \phi]\ (1 - S_{wH}), \qquad \text{(Eq. 5-16)}$$

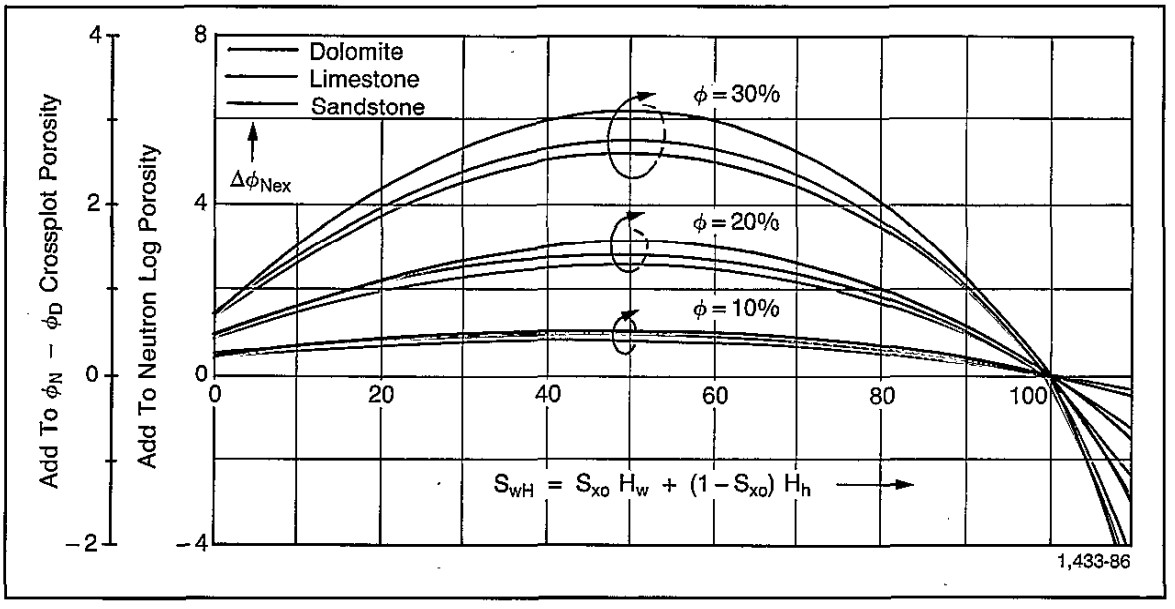


Fig. 5-24—Correction for excavation effect as a function of $S_{xo}$ for three values of porosity and for $H_g = 0$. Effects of limestone, sandstone, and dolomite included within the shaded bands.

where $\Delta\phi_{Nex}$, $\phi$, and $S_{wH}$ are in fractional units. For sandstone the coefficient, $K$, is 1; for limestone it is about 1.046, and for dolomite it is about 1.173. Note that the second term of this equation is rather small and can often be disregarded.

### Shales, Bound Water

Neutron tools see all hydrogen in the formation even if some is not associated with the water saturating the formation porosity. For example, it sees bound water associated with the shales. Shales in general have an appreciable hydrogen index; in shaly formations the apparent porosity derived from the neutron response will be greater than the actual effective porosity of the reservoir rock.

Also, the neutron tool measures water of crystallization. For example, nonporous gypsum ($CaSO_4 + 2H_2O$) has a large apparent porosity because of its significant hydrogen content.

### Effect of Lithology

The readings of all neutron logs are affected to some extent by the lithology of the matrix rock. SNP and CNL logs are usually scaled for a limestone matrix. Porosities for other lithologies are obtained from Chart Por-13 (Fig. 5-25) or from scales on the log headings. The SNP corrections apply only to logs run in liquid-filled holes. When the hole is gas filled, the lithology effect is reduced to a negligible level, and porosity may be read directly subject to limitations. Lithology corrections to the DNL log are also made using Chart Por-13. The SNP response is used for the epithermal neutron measurement, and the CNL response is used for the thermal neutron measurement.

### Determining Porosity From Neutron Logs

Subject to various assumptions and corrections, values of apparent porosity can be derived from any neutron log. However, certain effects, such as lithology, clay content, and amount and type of hydrocarbon, can be recognized and corrected for only if additional porosity information — from sonic and/or density logs — is available. Any interpretation of a neutron log alone should be undertaken with a realization of the uncertainties involved.

### SNP Corrections

Most of the SNP corrections (e.g., mud weight, salinity, borehole diameter, temperature) and the porosity computation are automatically performed in the tool instrumentation. However, because the SNP tool is a directional sidewall device, it averages the hydrogen concentration of whatever material lies in front of the pad, including the mudcake.(A chart for mudcake correction is provided on Chart Por-15a.) The pad is pressed against the hole wall with great force so that much of the softer mudcake is scraped away. Moreover, the backup pad is small and tends to cut through the mudcake. To get the mudcake thickness in front of the pad, take the difference between caliper reading and bit size. (Do not divide by two.)

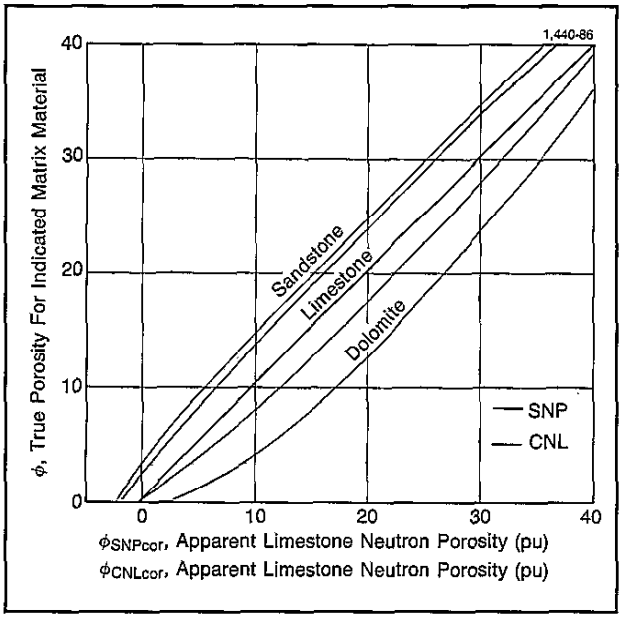


Fig. 5-25—Neutron porosity equivalence curves (Por-13a).

### Thermal Neutron Measurement

The CNL and DNL tools are designed to minimize the effects of hole size, mudcake, etc. on the thermal neutron measurement. When either tool is run in combination with the FDC tool, the caliper signal provides an automatic hole size correction. However, for the other perturbing influences, and for hole size when the FDC tool is not run, automatic correction is not possible because the variables are not measured or controlled. Moreover, some of these effects vary with porosity.

The standard conditions for CNL tool and DNL tool calibration are:

- 7⅞-in. borehole diameter
- Fresh water in borehole and formation
- No mudcake or standoff
- 75° F temperature
- Atmospheric pressure
- Tool eccentered in hole.

If there are departures from these conditions, the logs will require corrections. The combined correction for all

factors, usually small, yields a value of corrected neutron porosity index. Chart Por-14c provides the corrections to the CNL and DNL thermal neutron measurements for borehole size, mudcake thickness, borehole and formation-water salinities, mud weight, standoff, pressure, and temperature.

### Applications

Determining porosity is one of the most important uses of neutron logs. Corrections for lithology and borehole parameters are necessary for accurate porosity determinations.

The SNP log is specifically designed for open holes and provides porosity readings having minimum borehole effect. It can also be effectively used in gas-filled holes.

The compensation features of the CNL and Dual Porosity tools greatly reduce the effects of borehole parameters, and the tools are designed for combination with other openhole or cased hole tools. In combination with another porosity log (or other porosity data) or when used in a resistivity crossplot, the neutron log is useful to detect gas-bearing zones. For this application, the neutron-density combination is best in clean formations since the responses to gas are in opposite directions. In shaly formations, the neutron-sonic combination is an effective gas detector since shale affects each similarly. For greater accuracy in determining porosity and gas saturation in gas zones, the neutron log should be corrected for excavation effect.

The neutron log is used in combination with other porosity logs for lithology and shaly-sand interpretation. A comparison of the DNL epithermal neutron and thermal neutron measurements can identify shales and clays and other rocks containing neutron absorbers.

Also, count rates from the epithermal detectors of the DNL tool can be used for determining porosity in empty holes.

## LOGGING-WHILE-DRILLING FORMATION DENSITY AND POROSITY

A logging-while-drilling tool has been developed to provide density and porosity logs comparable in quality to those obtained with current wireline techniques. This device is called the Compensated Density Neutron (CDN*) since it combines the two most important nuclear measurements in one drill collar.

The density measurement employs two gain-stabilized, photomultiplier/crystal scintillation detectors. Low density "windows" in the drill collar enable spectroscopy methods to be employed. The formation's photoelectric absorption factor ($P_e$) is also measured and is used for lithology identification.

Use of a 1.5 Ci Cs137 source results in a statistical precision of about 0.01 g/cc for the density measurement at a rate of penetration (ROP) of 50 ft/hr. The measurement is made through "windows" in a full gauge stabilizer that minimizes borehole standoff effects. Residual density errors are accounted for by using the traditional "spine and ribs" compensation technique. An independent measurement of the mud density is made continuously in the downhole tool which provides useful additional information for the correction of borehole standoff effects.

The borehole-compensated thermal neutron measurement provides a high quality porosity log formulated in terms of the traditional near/far ratio-porosity transform. A 7.5 Ci AmBe source provides a statistical precision of about 0.5 pu at 30 pu formation porosity with an 8-in. borehole and an ROP of 50 ft/hr. An extensive set of laboratory measurements and mathematical modeling results have been used to quantify environmental effects on both the density and porosity measurements.

The density and $P_e$ response, and the neutron porosity log are similar to the wireline Litho-Density and CNL logs (Fig. 5-26).

The tool provides for efficient rig floor handling procedures and continues Schlumberger's commitment to nuclear source safety. Both the density and neutron sources are retrievable by conventional wireline fishing techniques, minimizing the possibility of having to abandon the source downhole in the event that the drill pipe becomes stuck (Fig. 5-27).

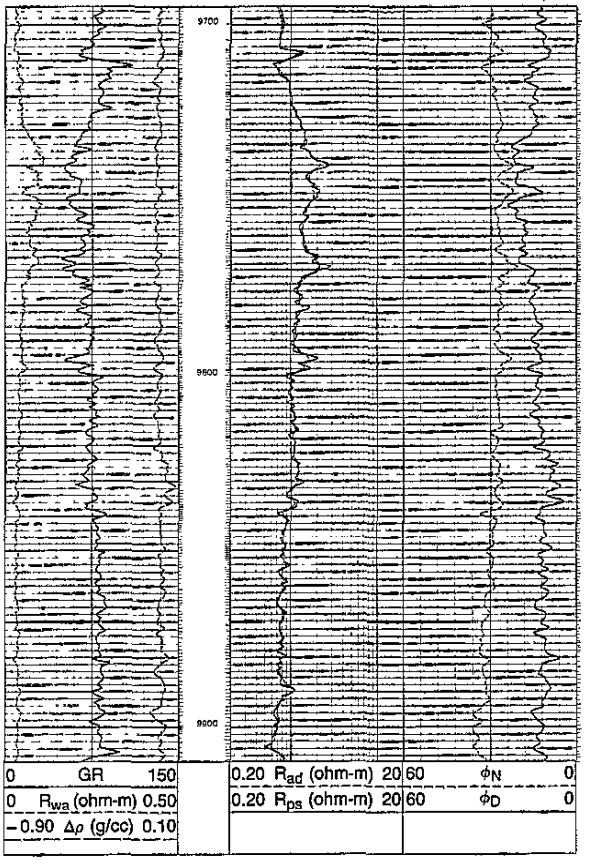


Fig. 5-26—Combined presentation of the CDN tool and the Compensated Dual Resistivity (CDR*) tool. Tick marks indicate the sampling rate of each measurement.

*Mark of Schlumberger

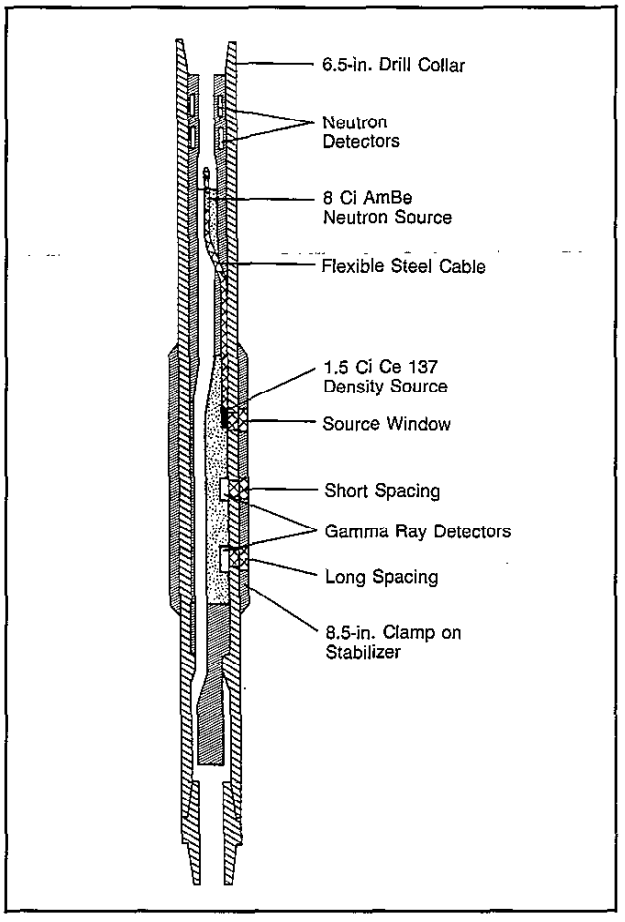


Fig. 5-27—Schematic of the CDN tool.

## REFERENCES


1. Kokesh, F.P. and Blizard, R.B.: "Geometric Factors in Sonic Logging," *Geophys.* (Feb. 1959) **24**, No. 1.
2. Kokesh, F.P., Schwartz, R.J., Wall, W.B., and Morris, R.L.: "A New Approach to Sonic Logging and Other Acoustic Measurements," *J. Pet. Tech.* (March 1965) **17**, No. 3.
3. Hicks, W.G.: "Lateral Velocity Variations Near Boreholes," *Geophys.* (July 1959) **XXIV**, No. 3.
4. Hicks, W.G. and Berry, J.E.: "Application of Continuous Velocity Logs to Determination of Fluid Saturation of Reservoir Rocks," *Geophys.* (July 1956) **21**, No. 3.
5. Wyllie, M.R.J., Gregory, A.R., and Gardner, G.H.F.: "Elastic Wave Velocities in Heterogeneous and Porous Media," *Geophys.* (Jan. 1956) **21**, No. 1.
6. Wyllie, M.R.J., Gregory, A.R., and Gardner, G.H.F.: "An Experimental Investigation of Factors Affecting Elastic Wave Velocities in Porous Media," *Geophys.* (July 1958) **23**, No. 3.
7. Tixier, M.P., Alger, R.P., and Doh, C.A.: "Sonic Logging," *J. Pet. Tech.* (May 1959) **11**, No. 5.
8. Pickett, G.R.: "Acoustic Character Logs and Their Applications in Formation Evaluations," *J. Pet. Tech.* (June 1963) **15**, No. 6.
9. Morris, R.L., Grine, D.R., and Arkfeld, T.E.: "Using Compressional and Shear Acoustic Amplitudes for the Location of Fractures," *J. Pet. Tech.* (June 1964) **16**, No. 6.
10. Aron, J., Murray, J., and Seeman, B.: "Formation Compressional and Shear Interval-Transit-Time Logging by Means of Long Spacing and Digital Techniques," paper SPE 7446 presented at the 1978 SPE Annual Technical Conference and Exhibition.
11. Raymer, L.L., Hunt, E.R., and Gardner, J.S.: "An Improved Sonic Transit Time-to-Porosity Transform," *Trans.*, 1980 SPWLA Annual Logging Symposium, paper P.
12. Leslie, H.D. and Mons, F.: "Sonic Waveform Analysis: Applications," *Trans.*, 1982 SPWLA Annual Logging Symposium, paper GG.
13. Morris, C.F., Little, T.M., and Letton, W.: "A New Sonic Array Tool for Full Waveform Logging," paper SPE 13285 presented at the 1984 SPE Annual Technical Conference and Exhibition.
14. Alger, R.P., Raymer, L.L., Hoyle, W.R., and Tixier, M.P.: "Formation Density Log Applications in Liquid-Filled Holes," *J. Pet. Tech.* (March 1963).
15. Tittman, J. and Wahl, J.S.: "The Physical Foundations of Formation Density Logging (Gamma-Gamma)," *Geophys.* (April 1965).
16. Wahl, J.S., Tittman, J., and Johnstone, C.W.: "The Dual Spacing Formation Density Log," *J. Pet. Tech.* (Dec. 1964).
17. Gaymard, R. and Poupon, A.: "Response of Neutron and Formation Density Logs in Hydrocarbon-Bearing Formations," *The Log Analyst* (Sept.-Oct. 1968).
18. Hottman, C.E. and Johnson, R.K.: "Estimation of Formation Pressures from Log-Derived Shale Properties," *J. Pet. Tech.* (June 1965).
19. Fertl, W.H. and Timko, D.J.: "Occurrence and Significance of Abnormal Pressure Formations," *Oil and Gas J.* (Jan. 5, 1970).
20. Fertl, W.H. and Timko, D.J.: "How Abnormal-Pressure-Detection Techniques are Applied," *Oil and Gas J.* (Jan. 12, 1970).
21. Gardner, J.S. and Dumanoir, J.L.: "Litho-Density Log Interpretation," Trans., 1980 SPWLA Annual Logging Symposium, paper N.
22. Ellis, D., Flaum, C., Roulet, C., Marienbach, E. and Seeman, B.: "The Litho-Density Tool Calibration," paper SPE 12084 presented at the 1983 SPE Annual Technical Conference and Exhibition.
23. Tittman, J.: "Radiation Logging," *Fundamentals of Logging*, Univ. of Kansas (1956).
24. Tittman, J., Sherman, H., Nagel, W.A., and Alger, R.P.: "The Sidewall Epithermal Neutron Porosity Log," *J. Pet. Tech.* (Oct. 1966).
25. Alger, R.P., Locke, S., Nagel, W.A., and Sherman, H.: "The Dual Spacing Neutron Log," paper SPE 3565 presented at the 1971 SPE Annual Technical Conference and Exhibition.
26. *Recommended Practice for Standard Calibration and Form for Neutron Logs*, API RP33, American Petroleum Institute (Sept. 1959).
27. Segesman, F. and Liu, O.: "The Excavation Effect," *Trans.*, 1971 SPWLA Annual Logging Symposium.
28. Davis, R.R., Hall, J.E., Flaum, C., and Boutemy, Y.L.: "A Dual Porosity CNL Logging System," paper SPE 10296 presented at the 1981 SPE Annual Technical Conference and Exhibition.
29. Scott, H.D., Flaum, C., and Sherman, H.: "Dual Porosity CNL Count Rate Processing," paper SPE 11146 presented at the 1982 SPE Annual Technical Conference and Exhibition.
30. Sherman, H. and Locke, S.: "Effect of Porosity on Depth of Investigation of Neutron and Density Sondes," paper SPE 5510 presented at the 1975 SPE Annual Technical Conference and Exhibition.
31. Edmundson, H. and Raymer, L.L.: "Radioactive Logging Parameters for Common Minerals," *Trans.*, 1979 SPWLA Annual Logging Symposium, paper O.
32. Flaum, C.: "Dual Detector Neutron Logging in Air-Filled Boreholes," *Trans.*, 1983 SPWLA Annual Logging Symposium, paper BB.
33. Galford, J.E., Flaum, C., Gilchrist, W.A., and Duckett, S.: "Enhanced Resolution Processing of Compensated Neutron Logs," paper SPE 15541 presented at the 1986 SPE Annual Technical Conference and Exhibition.
34. Gilchrist, A., Galford, J., and Soran, P., and Flaum, C.: "Improved Environmental Corrections for Compensated Logs," paper SPE 15540 presented at the 1986 SPE Annual Technical Conference and Exhibition.
35. *Log Interpretation Charts*, Schlumberger Well Services, Houston (1989).